ISSN 2079-1704. Хімія, фізика та технологія поверхні. 2023. Т. 14. № 3. С. 275-299

PACS 61.43.–j; 61.48.Gh;61.43.Gt;81.05.ue; 81.05.uf doi: 10.15407/hftp14.03.275

V.M. Gun'ko [1], Yu.I. Sementsov [1, 2], L.S. Andriyko [1], Yu.M. Nychyporuk [1], O.I. Oranska [1], O.K. Matkovsky [1], Yu.V. Grebel'na [1], B. Charmas [3], J. Skubiszewska–Zięba [3], M.T. Kartel [1, 2]

2D–NANOSTRUCTURED CARBONS: EFFECTS OF OXIDATION AND PACKING DISORDERING

[1] Chuiko Institute of Surface Chemistry of National Academy of Sciences of Ukraine
17 General Naumov Str., Kyiv, 03164, Ukraine, E–mail: vlad_gunko@ukr.net
[2] Ningbo University of Technology
No 55-155 Cui Bai Road, Ningbo, 315016, China
[3] Faculty of Chemistry, Maria Curie–Skłodowska University
3 Maria Curie–Skłodowska Sq., Lublin, 20–031, Poland

Various 2D carbons demonstrate significant effects of surface oxidation, heating, suspending–drying, cryogelation, swelling, and adsorption of polar and nonpolar compounds on the morphological, structural, and textural characteristics. Heating at 120–150 °C could result in collapse of pores not only between carbon sheets in stacks but also between neighboring stacks; therefore, the specific surface area (SSA) decreases by a factor of 30–100 for preheated graphene oxides (GO). According to the TEM and XRD data, the GO structure is rather amorphous, since only small X-ray coherent scattering regions demonstrate a certain order giving broad XRD (001) and (002) lines. In the Raman spectra, the D line (disordered defect structures with sp^3 hybridized C atoms) intensity for GO is similar to that of the G line (ordered structures with sp^2 hybridized C atoms). The graphite oxide (GtO) structure, which is closer to that of graphite than that of GO, is characterized by intensive G and low D lines, and the main XRD peak at 26.4° (characteristic for graphite) is broadened similar to the XRD peak of GO at 10°. Despite the GO stacks have a tendency to collapse upon heating, the collapsed stacks can be swollen not only in water (strongly) but also in liquid nitrogen (relatively weakly). Therefore, the use of GO in aqueous media can provide great SSA values in contact with the solvent and solute molecules. This could provide high efficiency of the GO use for purification of wastewater, separation of solutes, etc. MLGO produced from natural flake graphite as a precursor (flakes < 0.2 mm in size) using a modified method of ionic hydration and freeze–drying is characterized by typical light brown color, low bulk density, flexible sheet stacks easily collapsed, but its interaction with water results in strong swelling. Interaction between the carbon sheets in preheated MLGO is strong and nonpolar molecules, such as benzene, n–decane, poorly penetrate between the sheets, i.e., intercalation adsorption is small. However, water molecules can effectively penetrate (this is rather intercalation adsorption resulting in swelling) between the sheets, but the swelling effect of water adsorbed from the gas phase could be weaker than that in the aqueous suspensions. Thus, the proposed synthesis method of MLGO using natural graphite is effective and appropriate for preparation of the materials for various practical applications.

***Keywords**: graphene oxide, graphite oxide, exfoliated graphite, morphological characteristics, texture, structure, heating–cooling–drying effects, suspending effects*

INTRODUCTION

Various 1D (*e.g.*, nanotubes, nanofibers), 2D (graphene, graphene oxide, exfoliated graphite, graphite oxide), and 3D (graphite, activated carbons, carbon blacks, fullerites) carbons are important materials for industrial, medicinal, and other applications [1–9]. Such 2D carbons as single (SLG) and multi (MLG) layer graphenes, single (SLGO) and multi (MLGO) layer graphene oxides (GO), as well as thermally exfoliated graphite (EG), are very promising *per se* or as components of composites for various applications [8–15]. However, the graphene and GO materials remain relatively expensive (especially SLG and SLGO) despite significant reduction of their cost during last several years. Therefore, searching of less expensive pathways of preparation of 2D carbon materials is of interest from a practical point of view. One of these pathways could be based on natural cheap raw and relatively pure materials such as natural flake graphite treated, *e.g.*, using relatively cheap modified methods of preparation of graphite oxide (GtO) [16]. An additional way to reduce the final cost can be based on preparation of composites with graphene materials and other cheaper materials, *e.g.*, fumed oxides, natural

disperse minerals (*e.g.*, clays), polymers, *etc.* Note that previous investigations of carbon materials in combination with fumed silica showed that carbon layers can practically completely cover the silica surface [17]. The graphene materials could be used in composites with various metal oxides [18, 19].

For graphene (or GO) based composites, the fundamental properties and characteristics caused by a specific 2D structure of relatively large carbon sheets with significant amounts of O–containing functionalities in GO play an important role in adsorption of polar or nonpolar, low– or high–molecular weight compounds, reactions in the gas and liquid phases, electro–physical properties (*e.g.*, anisotropic electro–conductivity), structurization effects, *etc.* [20–35]. For GO, the surface O–containing functionalities determine the behavior of these carbons in both gaseous and liquid media or in composites even at low GO content due to a large specific surface area (SSA) [36–51]. The efficiency of applications of the graphene/GO materials depends strongly on control of the interfacial phenomena at their surfaces because these materials are very flexible and soft and can be collapsed and agglomerated or deagglomerated during heating, evacuation, suspending with changes in pH value of the solutions, presence of bound oxide or metallic nanoparticles, *etc.* [1–21,52–59]. Composites with GO and various metal oxides can be used as effective catalysts, adsorbents, polymer fillers, *etc.* [60–68], and interfacial phenomena play an important role in these composites *per se* and, therefore, in their applications. Preparation of a monolayer (or close) carbon coverage of various matrices (carriers) is of interest from both theoretical and practical points of view because the matrices could be much cheaper than GO but the surface properties of the composites may be determined by the GO layers. Interactions of the graphene materials with water and various aqueous solutions and suspensions are of importance because these materials are frequently used in the aqueous media. Features of these interactions depend on many factors such as types of dispersion media (humid air, aqueous or more complex media, pH, salinity, *etc.*), content and structure of solutes or adsorbates and co–adsorbates, temperature, mechanical loading, aging, *etc.* Therefore, investigations of the interfacial phenomena, as well as the morphological, structural and textural characteristics, are of importance to control the properties of the graphene/GO materials in different media under different conditions, and these investigations were aimed in the present work dealing with GO, EG, and GtO for a deeper insight into the above-mentioned problems.

MATERIALS

Several 2D carbons were used in this study: commercial single–layer (SLGO with 1–3 layers) and multi–layer (MLGO with 5 or more layers) graphene oxides (Cheap Tubes, Inc.), MLGO prepared using natural graphite and several preparation methods, cryo–MLGO after cryogelation of 5 % aqueous suspension of MLGO in a cryo–reactor at 260 K, 1050 atm, for 24 h and subsequent drying in air for a week, two samples of thermally exfoliated graphite (EG, S_{BET} = 21 m^2/g and TEG, S_{BET} = 39 m^2/g), and graphite oxide (GtO). MLGO with natural flake graphite (Zaval'evsk coal field, Ukraine; flake sizes < 0.2 mm) as a precursor was prepared using a modified method of ionic hydration described in detail elsewhere [16, 69]. Briefly, a solution of concentrated H_2SO_4 (0.65 L) with $KMnO_4$ (72 g) added by small portions during constant stirring was added to 20 g of flake graphite and heated at 45 °C to appearance of blue color of graphite bisulfate and cooled to 10–15 °C. Then the mixture was heated to 400 °C. It was stirred to a slurred state and then aged for 20 h at room temperature. Water (120 mL) was added with constant stirring at 45 °C. The mixture was maintained at 45 °C for 1 h, cooled to 10–15 °C, and 1 L of water was added, and then 70 mL of 28 % H_2O_2 was added by small portions with constant stirring. The obtained mixture of light–yellow color was centrifuged. The residue was suspended in 3 % aqueous solution of HCl (2 L) and again centrifuged. Then, the residue was suspended in bidistilled water and centrifuged, and this procedure was repeated four–five times to neutral pH of the suspension. The dried residue after final centrifugation was freeze–dried at –24 °C to 25 °C at 10^{-3} Torr. The MLGO samples were also dried and degassed by evacuation up to 10^{-3} Torr. The final dry MLGO has very low bulk density and light brown color similar to that of commercial MLGO or SLGO (Cheap Tubes, Inc.) used in comparative investigation with MLGO

produced from natural flake graphite (see some details elsewhere [35, 45, 54, 69]).

For preparation of other samples of graphene oxide (MLGO), anodic oxidation of thermally exfoliated graphite (TEG, S_{BET} = 39 m^2/g) foil (Ukraine standard – TU 26.8–30969031–002–2002) being in a low–concentrated aqueous solution of KOH [70] was applied. As a precursor of TEG, intercalated graphite (Ukraine standard – TU 14.50.9–30969031–001–2002) was prepared by anodic oxidation of natural graphite (GtO). This procedure with two consecutive controlled electrochemical processes allows us to adjust the TEG structure with cluster–assembled nanoscale system [71, 72], and then, the size and surface state of MLGO [70].

CHARACTERIZATION METHODS

High resolution transmission electron microscopy (HRTEM) images were recorded using JEM–2100F (Japan). A powder sample was added to acetone (for chromatography) and sonicated. Then a drop of the suspension was deposited onto a copper grid with a thin polymeric film. After acetone evaporation, sample particles remaining on the film were studied with HRTEM. The particle size distribution (PaSD) functions using TEM images was computed using Fiji (ImageJ) software with a local thickness plugin [73].

Atomic Force Microscopic (AFM) images were obtained by means of a NanoScope III (Digital Instruments, USA) apparatus using a tapping mode AFM measurement technique.

X–ray diffraction (XRD) measurements were performed using a Siemens D 5000 powder diffractometer and a DRON–4–07 diffractometer (Burevestnik, S.–Petersburg) with Ni-filtered CuK_a radiation (λ = 0.15418 nm) in step scan mode (2θ step size 0.04°, counting time 2 s per step, 2θ range of 2–80° but shown in the range of 5–60° or 5–70°). To identify the structure of synthesized deposits, obtained patterns were compared to those of known compounds from the JPCDS–ISDD (Joint Committee on Powder Diffraction Standards–International Centre for Diffraction Data) files. A method used for calculations of the size distribution functions of ordered fragments (*i.e.*, X-ray coherent scattering regions, CSR) in sheets on the basis of full profile analysis of XRD patterns (using a regularization procedure with such models of particles as lamellar and spherical ones) was described in detail elsewhere [74, 75]. Note that the X-ray CSR of 1–2 nm in size could be observed even in such amorphous materials as fumed silica. For ordered fragments in the carbon sheets of GO, the CSR conception is more appropriate than that of nano-crystallites because the latter have own boundaries but the former do not have, *e.g.*, in the carbon sheets which are continuous.

Low–temperature (77.4 K) adsorption–desorption of nitrogen was measured for preheated and degassed samples using a Micromeritics ASAP 2420 adsorption analyzer. The pore size distributions (PSD) were calculated using nonlocal (NLDFT), quenched solid (QSDFT) density functional theory [76], or DFT [75] methods.

Thermogravimetric (TG and differential TG, DTG) measurements with differential thermal analysis (DTA) were carried out in an inert (nitrogen) atmosphere at 20–1200 °C using a Derivatograph C (Paulik, Paulik & Erdey, MOM, Budapest) apparatus. Samples of 25–28 mg were placed in a ceramic crucible heated at a heating rate of 10°C/min. Desorption of water and others was studied using the TG/DTA method.

Raman spectra of carbons were recorded using a Raman microscopy (inVia Reflex Renishaw, UK).

Infrared (IR) spectra of thin films of freeze–dry MLGO mixed with KBr (1:100, treated in a micro–grinder for 3 min) or after drying (in air) of aqueous suspension (6 wt. %) of MLGO were recorded using a Specord M80 (Carl Zeiss) spectrophotometer.

To analyze the interaction of water with 2D carbons and the presence of O–containing functionalities, desorption of water, CO, CO_2 and O was studied at a heating rate β = 1.93 K/s using a method of one–pass (OP) temperature-programmed desorption (TPD) time–of–flight (ToF) with mass-spectrometry (MS) control (pressure in a chamber 8×10^{-5} Pa, sample weight 0.5 mg, with a short distance (~0.5 cm) between a sample and a MS detector) with a MSC–3 (“Electron”, Sumy, Ukraine) ToF mass–spectrometer [77].

Particle size distributions were studied using a Zetasizer Nano ZS (Malvern Instruments) apparatus. Distilled water with the amounts of MLGO of 0.05 or 0.5 wt. % was utilized to prepare the suspensions sonicated for 2–10 min

using an ultrasonic disperser (Sonicator Misonix, power 500 W and frequency 22 kHz). The pH value was constant of 2.26 (C_{MLGO} = 0.5 wt. %) or 2.9 (C_{MLGO} = 0.05 wt. %). These relatively low values of pH are due to the presence of the COOH groups in the MLGO structure, as well as residual amounts of acids used on the material preparation.

To analyze the adsorption characteristics of MLGO with respect to polar and nonpolar adsorbates, the adsorption of water and benzene was studied using an adsorption apparatus with a McBain–Bark quartz scale at 293 K. Samples were evacuated at 10^{-3} Torr and 473 K for several hours to a constant weight, then cooled to 293±0.2 K, and the adsorption of water or benzene was studied at varied relative pressures p/p_s. The measurement accuracy was $1±10^{-3}$ mg with a relative mean error of ±5 %.

Differential scanning calorimetry (DSC) investigations of interactions of MLGO with nonpolar (benzene, toluene, and *n*–decane) and polar (water and DMSO) or a mixture of water and *n*–decane adsorbates were carried out using a PYRIS Diamond (Perkin Elmer Instruments, USA) differential scanning calorimeter calibrated at different heating rates using standard samples such as distilled water (melting temperature T_m = 0 °C) and indium (T_m = 156.6 °C) supplied by the producer and using the recommended standard calibration procedure.

A structure with two GO layers was computed by the MM+ method with the VEGA ZZ 3.2.2 program suit [78]. The model geometry was drawn using the UCSF ChimeraX package (version 1.5) [79]. The geometry of two–sheet model of graphene was also optimized using the PM7 method (MOPAC 2022, ver. 22.06) [80].

RESULTS AND DISCUSSION

The particulate morphology of 2D carbons studied depends not only on their kind (*e.g.*, GO, GtO, EG) but also on treatment conditions (heating, pressing, suspending at different pH, cryogelation, swelling, *etc.*) (Figs. 1–5). According to AFM images, the SLGO sheet surface is less smooth (Figs. 1 *a*, *b* and 2) than that of graphite (Fig. 1 *c*) due to strong oxidation, pretreatments of GO at various conditions, and flexibility of the carbon sheets alone or in thin stacks. Surface "waves" and other secondary structures observed in SLGO could be of several nanometers or larger (Figs. 1 and 2) that depend on preheating, suspending, and other treatments of the materials (Figs. 1–5). The GO sheet flexibility leads to the formation of various folds (Figs. 3 and 5). After suspending and drying, the morphology of secondary GO structures could be from biplicate structures (Fig. 3 *d*) to various stacks (Figs. 3 *c* and 4) depending on the characteristics of the dispersion media [35, 45, 54, 69, 81]. Thus, the particulate morphology of the GO materials could be rather unstable with significant variability appearing in various measurements because the pretreatment conditions could be also varied depending on a type of used equipment.

SLGO and MLGO (Cheap Tubes, Inc.), as well as GO, prepared using natural flake graphite as a precursor, and EG, demonstrate relatively large micro-scaled carbon sheets (Figs. 1–5) with a short–range order in nano-scaled structures, clusters (Figs. 3 *b*, *f* and 4–7). HRTEM images show that the carbon structure in GO is rather amorphous due to a high level of the oxidation (~ 10 % of oxygen). Additionally, there are ash particles (Fig. 5 *c*, *d*), which composed mainly of carbon with a certain content of silica and other minor admixtures characteristic, *e.g.*, for natural graphite [69]. These particles can enhance the GO sheets disorder. Similar ash particles can be found in commercial GO (Cheap Tubes Inc.) [35, 45, 54, 81]. Note that the commercial GO are more amorphous than ones produced from natural flake graphite (Figs. 3 and 5–7) due to the differences in the precursors and preparation routes.

In contrast to GtO with O–functionalities decorating mainly the sheet edges, a large number of O–containing functionalities chemically attached to a total surface of carbon sheets of GO results in significant diminution of a peak at $2\theta \approx 26.4°$ (Fig. 6 *a*) characteristic for graphite [83]. It is practically absent in the initial SLGO pattern (Fig. 6 *a*) because SLGO is composed of very thin stacks of 1–3 layers with strongly destroyed graphite motives. However, after suspending (especially at pH 14) and drying of SLGO, this peak appears, but it is broadened in comparison to that of GtO (Figs. 6 *a* and 7 *a*). For GtO, certain broadening of this peak is also observed (due to certain amorphism of oxidized graphite), but for GtO, there is no a peak at $2\theta \approx 10°$ characteristic for GO with *d*–spacing of 0.7–1.0 nm corresponding to the size of the stacks

with 2–3 layers (Fig. 6 *b*). After suspending–drying of SLGO, a broad peak appearing at $2\theta \approx 26.4°$ (Fig. 7) depends on pH value of the suspension. The suspending-drying results in changes in the ordered fragments (*i.e.*, X-ray coherent scattering regions, CSR) in the sheets (Fig. 7 *c*) significantly different from those for initial GO (Fig. 6 *c*). These effects could be explained by removal of a fraction of acidic O–containing functionalities of SLGO in strongly basic solution at pH 14 (Fig. 7, curve 2) and a weaker effect in the acidic solution at pH 1 (curve 1).

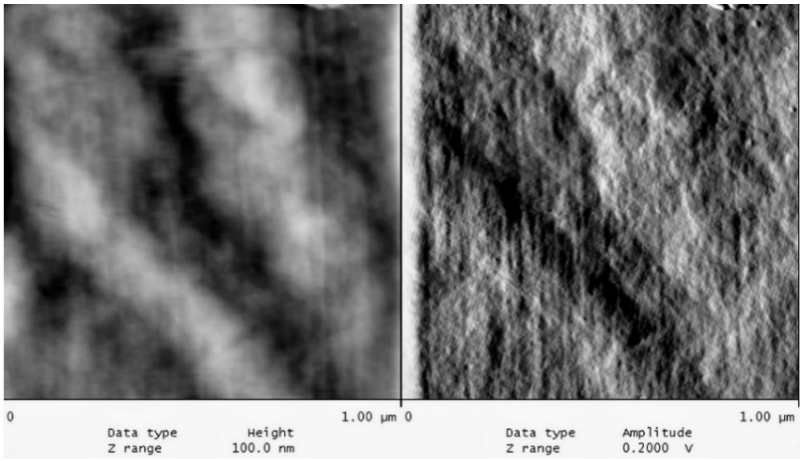

a

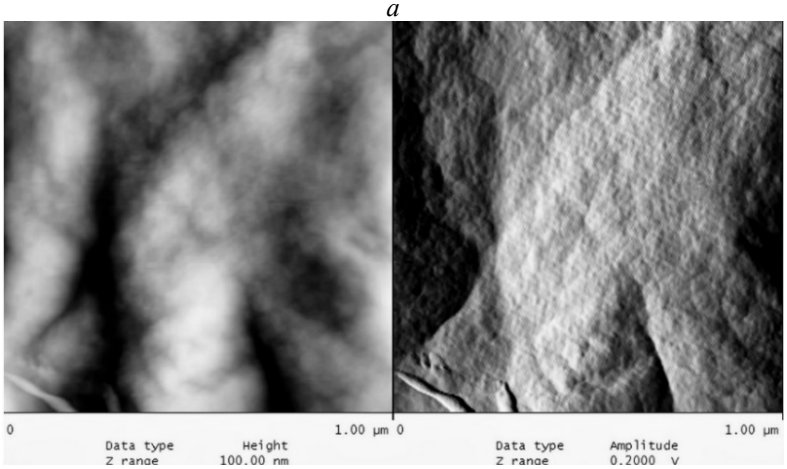

b

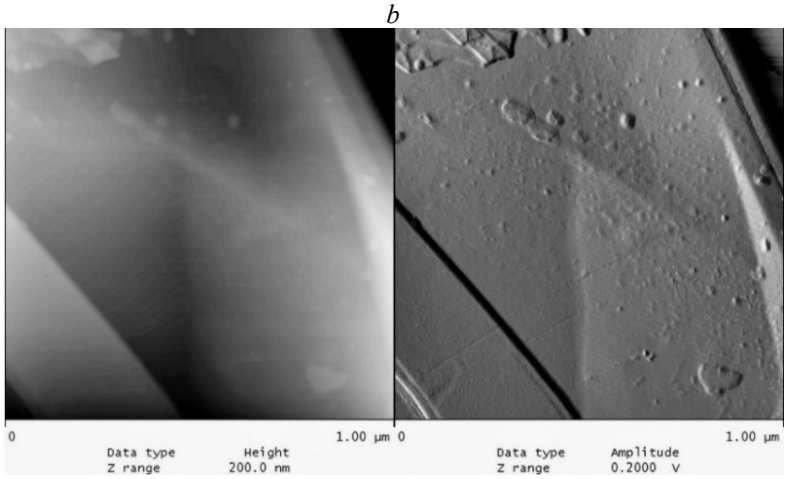

c

Fig. 1. AFM images of (*a*) initial and (*b*) preheated (at 150 °C) SLGO (Cheap Tubes, Inc.) and (*c*) natural graphite (image sizes are 1×1 µm^2)

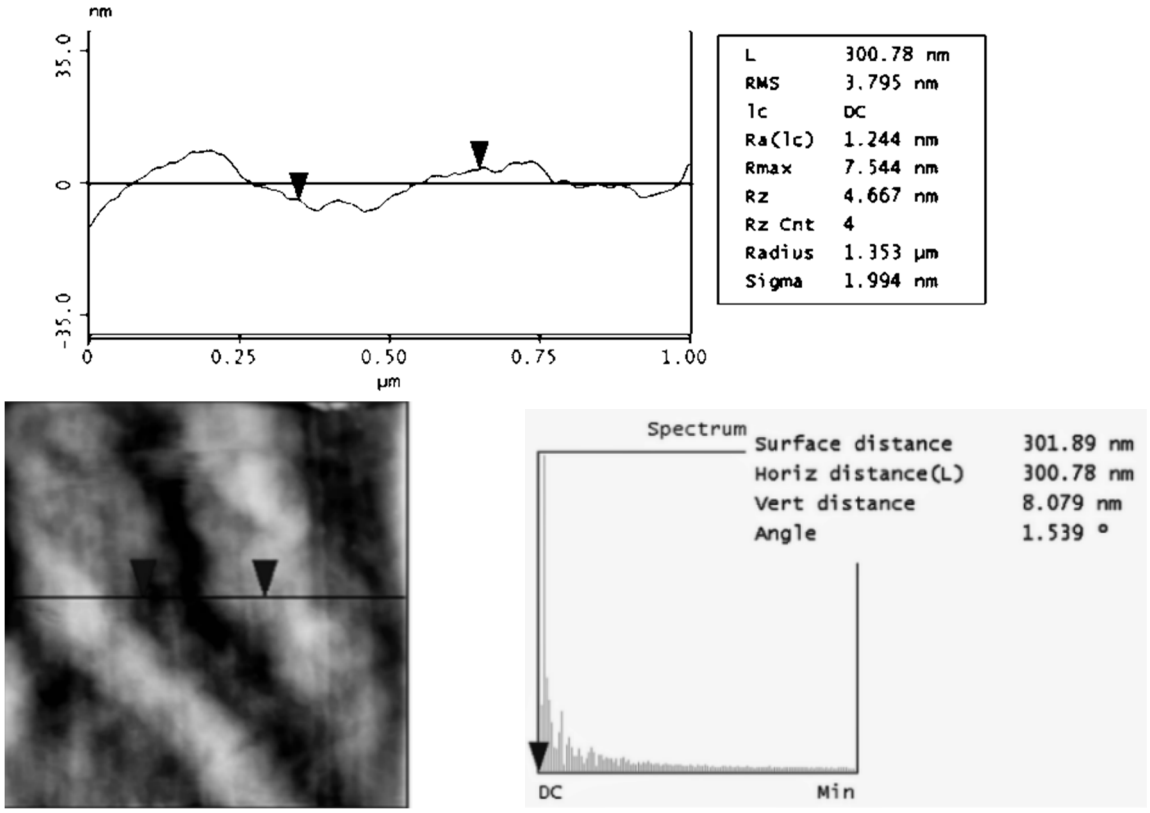

a

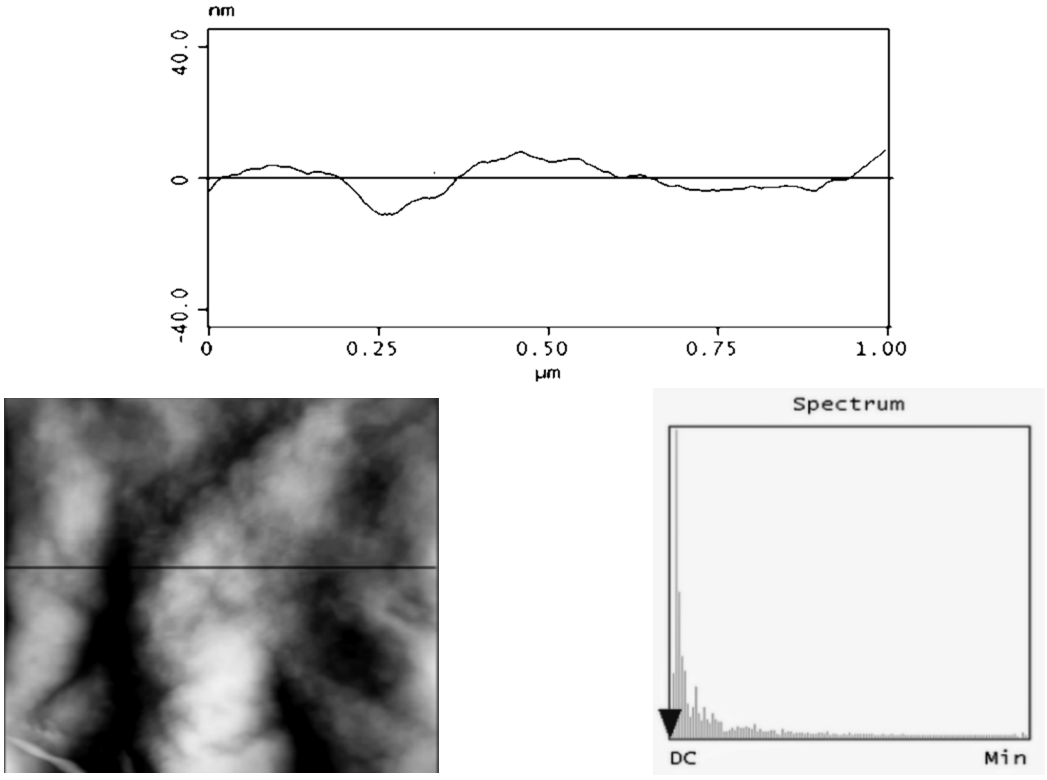

b

Fig. 2. Height profile analysis using AFM images of (*a*) initial and (*b*) preheated SLGO (Cheap Tubes, Inc.)

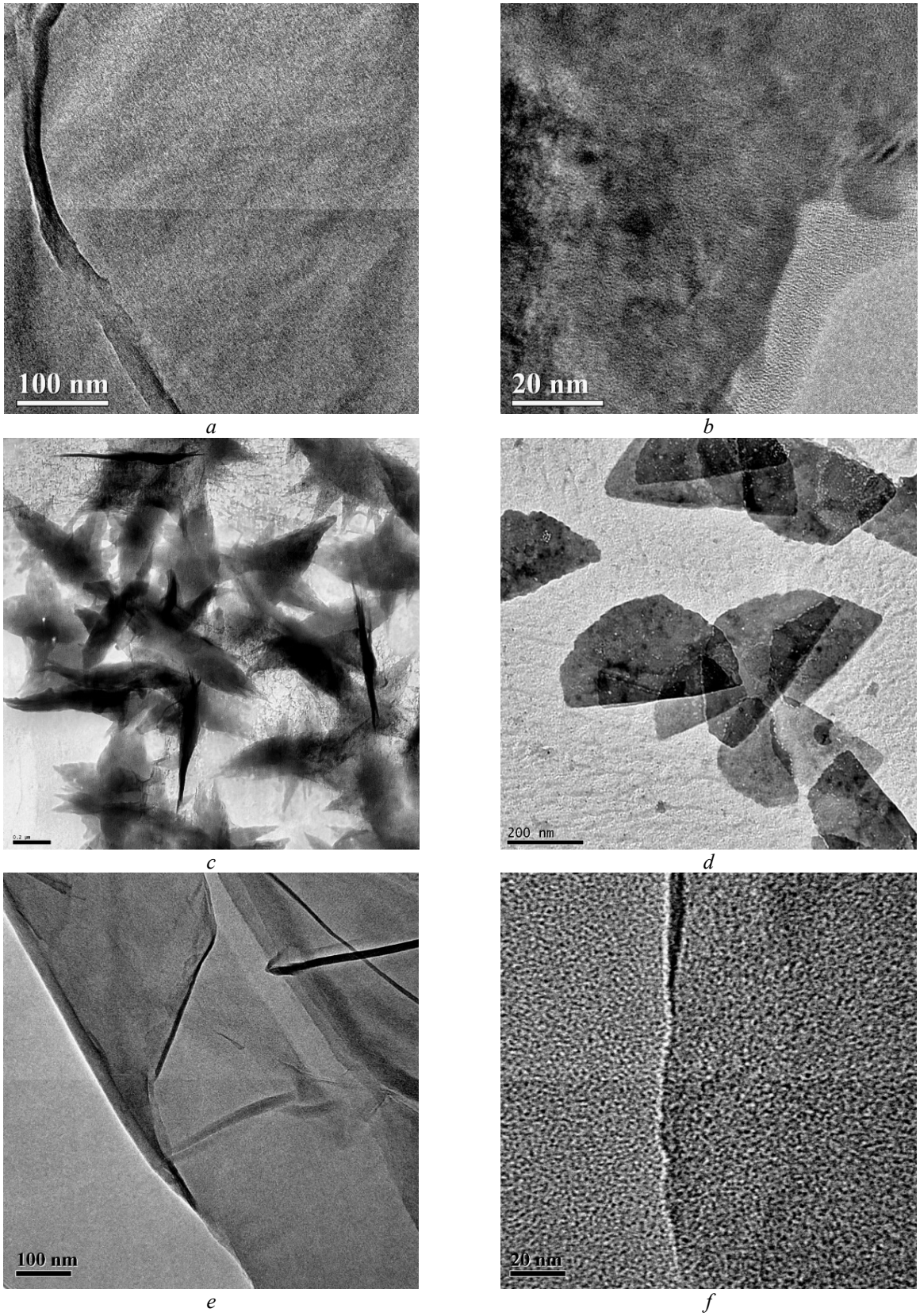

a *b* *c* *d* *e* *f*

Fig. 3. TEM images of SLGO (*a*, *b*) initial and (*c*, *d*) suspended at pH (*c*) 7 and (*d*) 3 and (*e*, *f*) initial MLGO (both GO from Cheap Tubes, Inc.) (some details are in [35, 45, 54, 81]) (scale bar (*a*, *e*) 100, (*b*, *f*) 20 and (*c*, *d*) 200 nm)

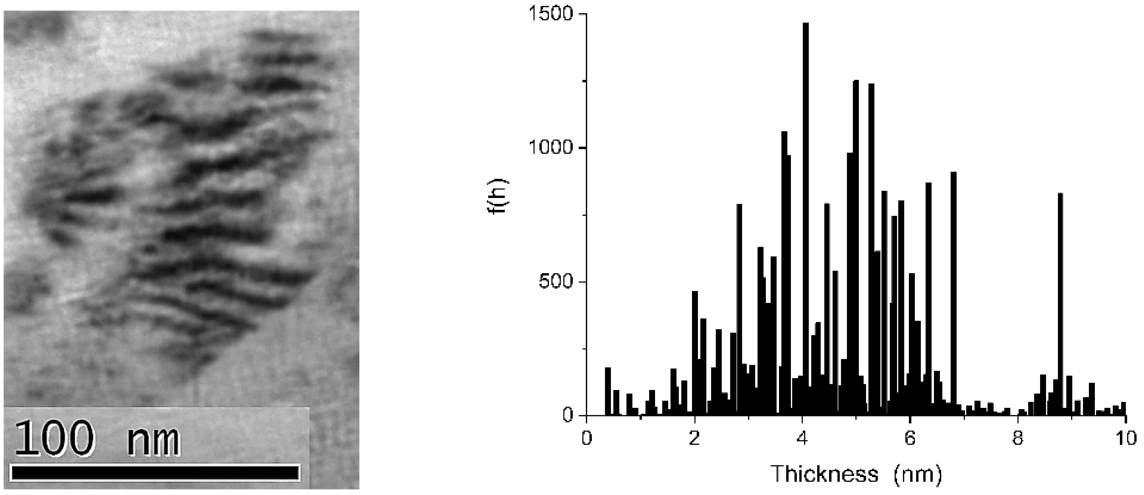

Fig. 4. A fragment of TEM image of SLGO (Cheap Tubes, Inc.) suspended at pH 7 and dried (scale bar 100 nm) and related thickness distribution $f(h)$ in the 0.5–10 nm range

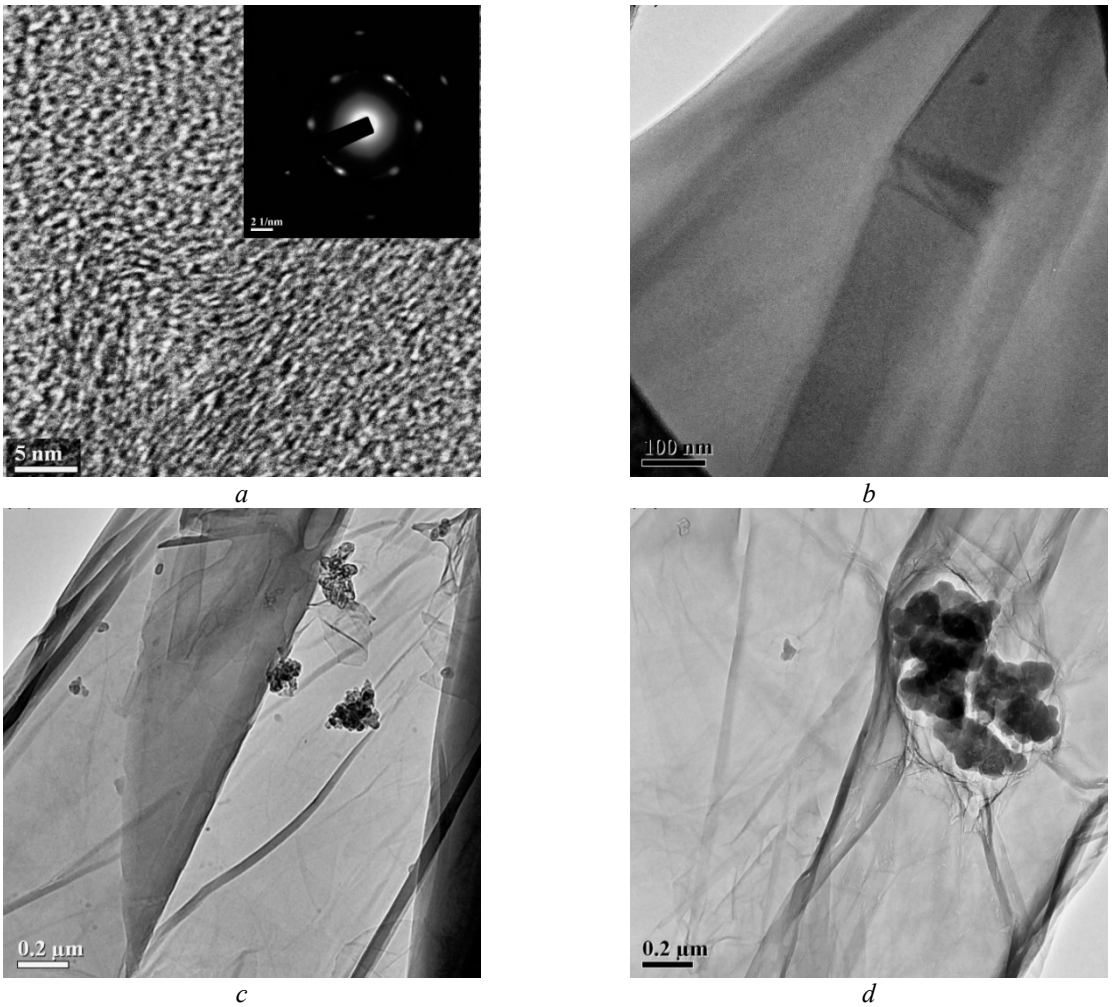

a *b* *c* *d*

Fig. 5. TEM images of freeze–dry MLGO prepared using natural flake graphite at different magnifications of (*a*, *b*) pure carbon sheets and (*c*, *d*) multi–layer structures with ash particles (scale bar (*a*) 5, (*b*) 100, and (*c*, *d*) 200 nm) (see additional information in [69])

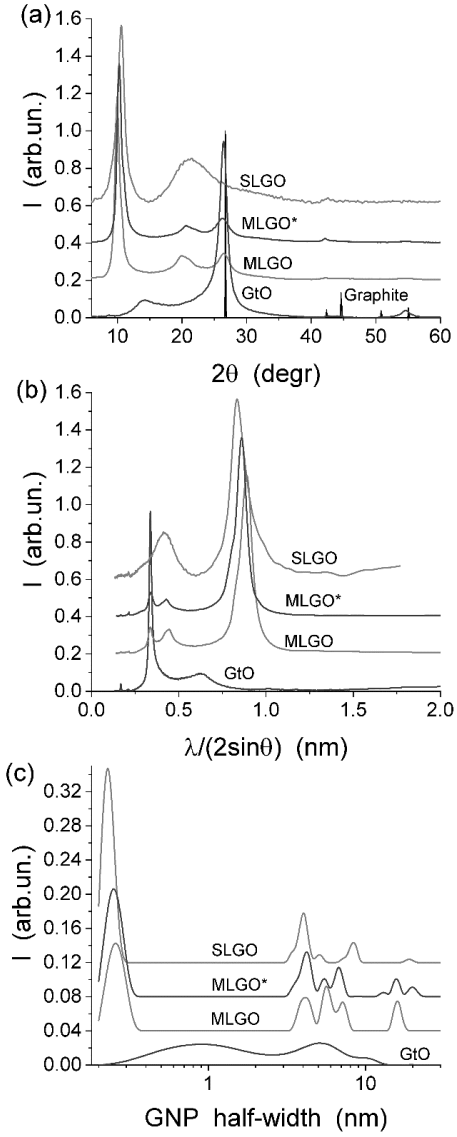

Fig. 6. (*a*) XRD patterns, (*b*) d–spacing, and (*c*) CSR size distributions for initial SLGO (Cheap Tubes, Inc.), freeze–dry MLGO* and vacuum–dried MLGO prepared using natural graphite, and graphite oxide (GtO)

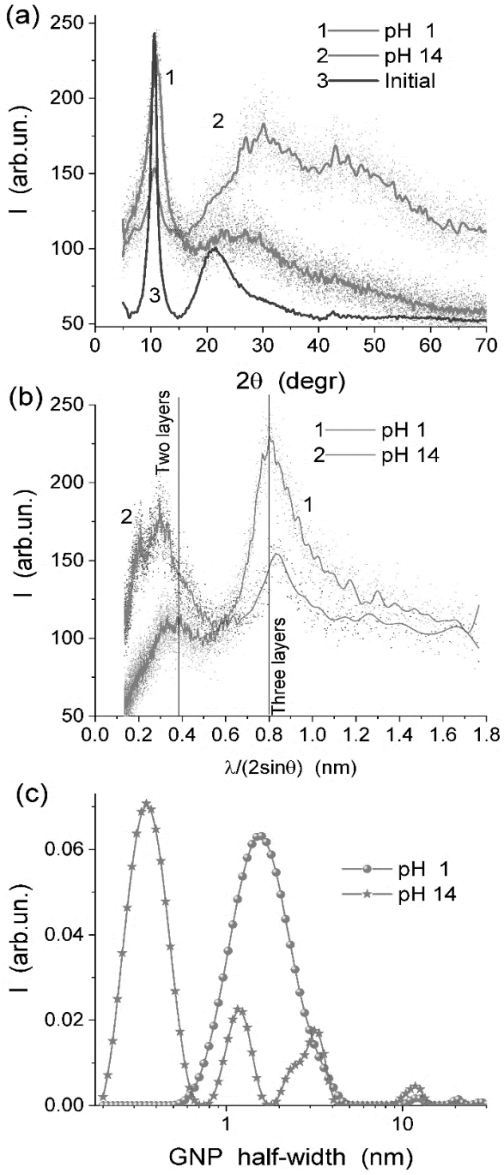

Fig. 7. (*a*) XRD patterns, (*b*) d–spacing, and (*c*) CSR size distributions for SLGO dried after suspending at pH 1 and 14; (*a*) XRD pattern for initial SLGO (curve *3*)

Thus, the GO structure is not stable upon treatments under various conditions. This is also confirmed by the preheating effects on the textural characteristics. For example, SLGO preheated at 150 °C demonstrates diminution in the porosity and specific surface area (SSA) (Table 1) in comparison with the SSA value expected as *ca.* 1500 m^2/g for intact SLGO [35, 45, 54, 69, 81]. On the other hand, for GO treated in liquid media, the SSA value in contact with liquids could be 400–1000 m^2/g due to significant swelling effects [69] (*vide infra*).

The textural instability of GO is clearly visible from comparison with exfoliated graphite, since GO is significantly swollen even in liquid nitrogen (open hysteresis loop remains at low pressure, as well as upon the water adsorption, *vide infra*), but EG does not demonstrate a similar hysteresis effect (Fig. 8 *a*). SLGO is characterized by a significant contribution of narrow slit–

shaped nanopores (pore half–width x < 1 nm) between sheets in stacks in contract to two samples of EG composed of thicker stacks (Figs. 8 *b* and 9). These results are in agreement with the Raman spectra of SLGO and EG samples (Fig. 10) since the D line (caused by sheet defects with sp^3 hybridized C atoms) is weak for EG in comparison to the G line (sp^2 hybridized C atoms) in contrast to SLGO having intensive both lines. This is due to the effects of O–containing functionalities bonding mainly with sp^3 hybridized C atoms at the total surface of the sheets (see models below).

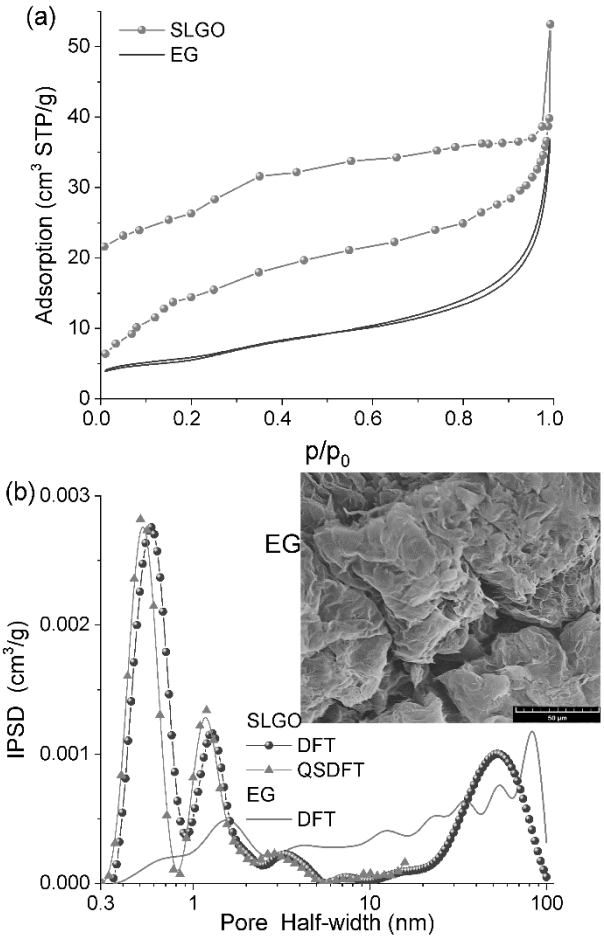

Fig. 8. (*a*) Nitrogen adsorption–desorption isotherms and (*b*) incremental pore size distributions for preheated SLGO and exfoliated graphite, EG (DFT [75, 82], quenched solid DFT (QSDFT) [73]). EG morphology is shown in scanning electron microscopy image (SEM, Quanta 3D FEG (FEI), voltage 15 kV, scale bar 50 μm) in insert

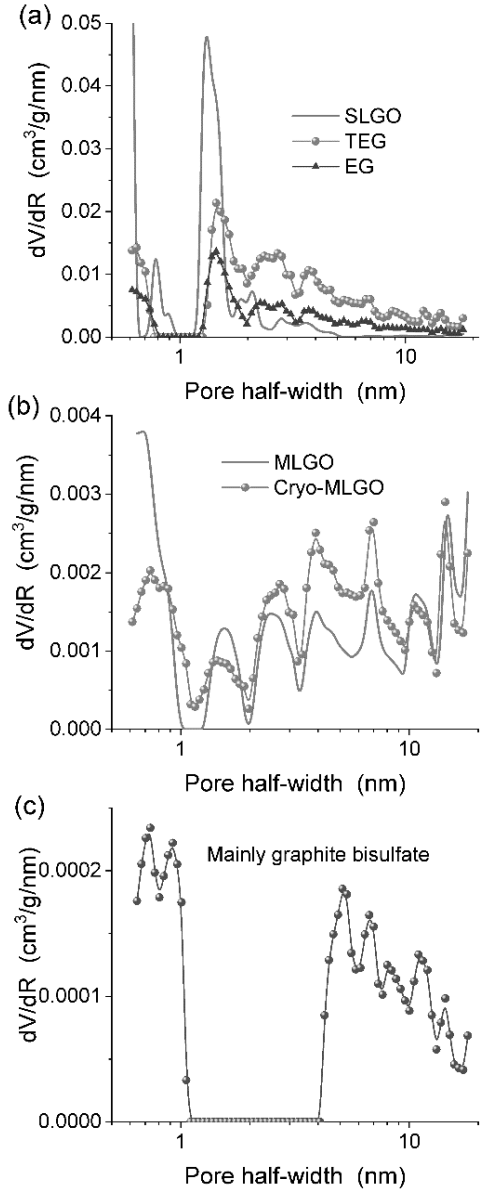

Fig. 9. NLDFT PSD for 2D carbons: (*a*) SLGO (Cheap Tubes, Inc.), TEG, EG, (*b*) initial MLGO and cryo–MLGO, and (*c*) graphite bisulfate

Table 1. Textural characteristics (SSA and pore volume, V_p) of 2D carbons preheated at 150 °C with collapsed GO stacks

Sample	S_{BET} (m^2/g)	S_{NLDFT} (m^2/g)	V_p (cm^3/g)
MLGO	9	7	0.05
cryo–MLGO	7	6	0.05
Gt–bisulfate	0.2	0.4	0.003
EG	21	16	0.06
TEG	39	33	0.15
SLGO	57	86	0.08

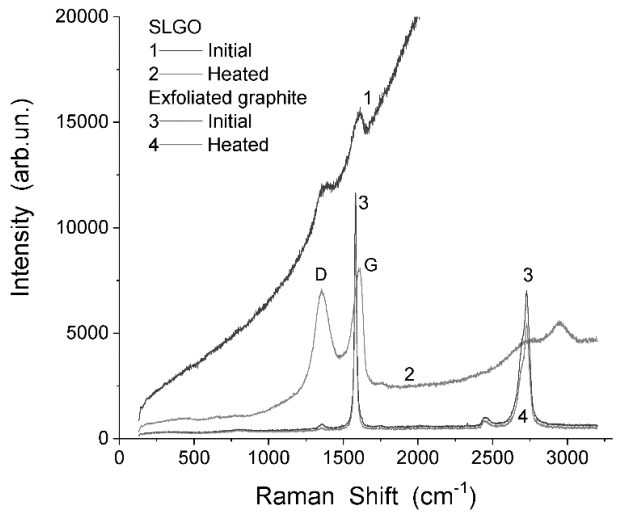

Fig. 10. Raman spectra of SLGO and EG initial and preheated at 150 °C

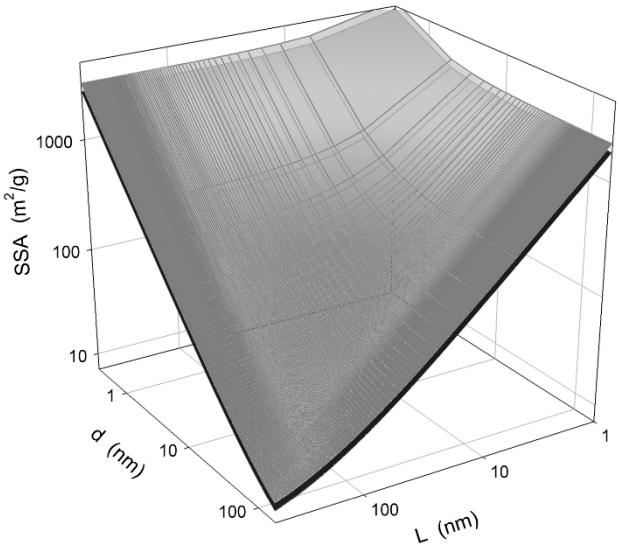

Fig. 11. Model calculations of the SSA value *vs*. sizes of graphene sheets ($L \times L$) and stack thickness (d) for graphene (lower surface) and GO (upper surface) estimated for individual stacks

For 2D carbons, the SSA value depends strongly on the sizes of sheets and stacks (Fig. 11). The SSA values for studied samples (Table 1, S_{BET} and S_{NLDFT}) show that the particulate morphology corresponds to relatively large sheets and stacks for preheated 2D carbons (Figs. 1–5), observed also after suspending–drying (Fig. 3 *c*).

According to the chemical analysis (with EDAX) of MLGO [69], it contains approximately 11 at. % of oxygen (that is typical value for GO), which appears in different O–containing functionalities (Fig. 12, Table 2). This value is similar to that for commercial GO (~ 10 %), and it is in agreement with the weight loss (taking into account the desorption of intact water molecules) observed during heating of MLGO from 220 to 1200 °C in the inert atmosphere (Fig. 13). The TG/DTG/DTA data (Fig. 13) show, at least, five desorption/decomposition processes occurring at different temperatures and resulting in 16 wt. % loss upon heating to 1200 °C in the inert atmosphere. This weight loss is larger than the content of oxygen in GO because a part of the C atoms removed with the O atoms as CO and CO_2 upon decomposition of the surface functionalities (Figs. 12 and 14). These results are in agreement with the TPD MS data (Fig. 15) (*vide infra*).

The IR spectra of MLGO (Fig. 12, Table 2) are in agreement with the data on GO analyzed in detail elsewhere [84]. In the IR spectra, there are bands related to various O–containing functionalities (see Table 2 and models in Fig. 14 showing flexible GO fragments dry and hydrated), which play a predominant role in interfacial phenomena studied here (*vide infra*). Some IR bands demonstrate decreasing splitting after suspending and drying (Fig. 12, comp.

curves 2 and 1). Additionally, the amount of strongly bound water (3200–2500 cm^{-1}) increases for the second sample. These results show than suspending and simple drying in air lead to strong aggregation of the carbon sheets in large stacks.

According to TPD MS data, the main portion of the oxygen in MLGO (studied as a representative of various oxidized 2D carbons), corresponding to attached surface functionalities, starts to be intensively decomposed at approximately 500 °C and higher (Fig. 15). The line of CO, corresponding to decomposition of carboxylic, epoxy, and other functionalities with one O atom per group, is more intensive than line CO_2 formed due to decomposition mainly of the groups with two O atoms per group or bimolecular reactions of two neighboring groups. Water is intensively desorbed at lower temperatures due to the presence of intact water molecules (responsible for molecular desorption occurring at lower temperatures than associative one, the first DTG extremum in Fig. 13) and OH groups participating in associative desorption at higher temperatures (second DTG extremum in Fig. 13). The position of the main peaks at 480–500 K (Fig. 15) is similar to that of the second DTG peak at 200 °C (Fig. 13). Peaks of CO_2 and H_2O (Fig. 15) have close positions due to bimolecular reactions of the O-containing groups with the elimination of H_2O and CO_2. The decomposition of the epoxy groups can strongly contribute the O and CO lines. The lines of H_2O (toward lower temperatures) and CO (toward higher temperatures) are broader those that of O and CO_2 (Fig. 15) because of a larger number of sources for the former than for the latter.

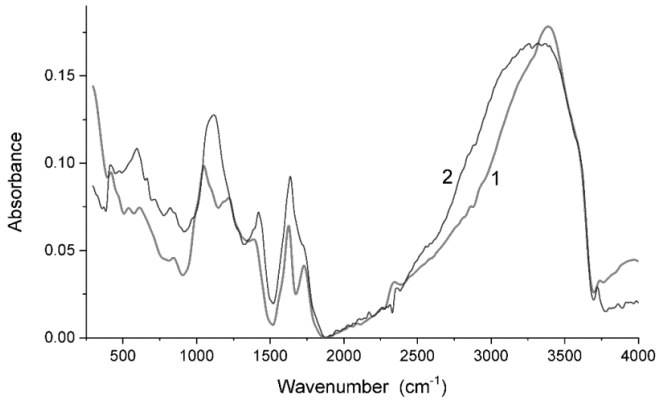

Fig. 12. Infrared spectra of freeze–dry MLGO mixed with dry KBr (1:100, treated in a micro–grinder for 3 min) (curve *1*) or suspended (6 wt. % aqueous suspension) and dried in air to form a very thin film (curve *2*) (see details in [69])

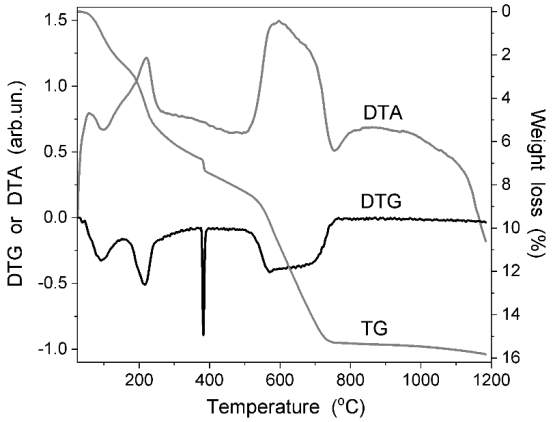

Fig. 13. TG/DTG/DTA thermograms of MLGO (from natural graphite) heated in inert atmosphere (see details in [69])

Table 2. Assignment of the IR bands of MLGO

Band (cm^{-1})	Assignment
3700–2500	O–H (surface hydroxyls, H_2O)
2890–2800	C–H
1730	C=O
1630	COOH, C=O, H_2O
1425, 1394	C=C, C–O–H
1225	C–O–C
1115, 1040	C–O, C–C

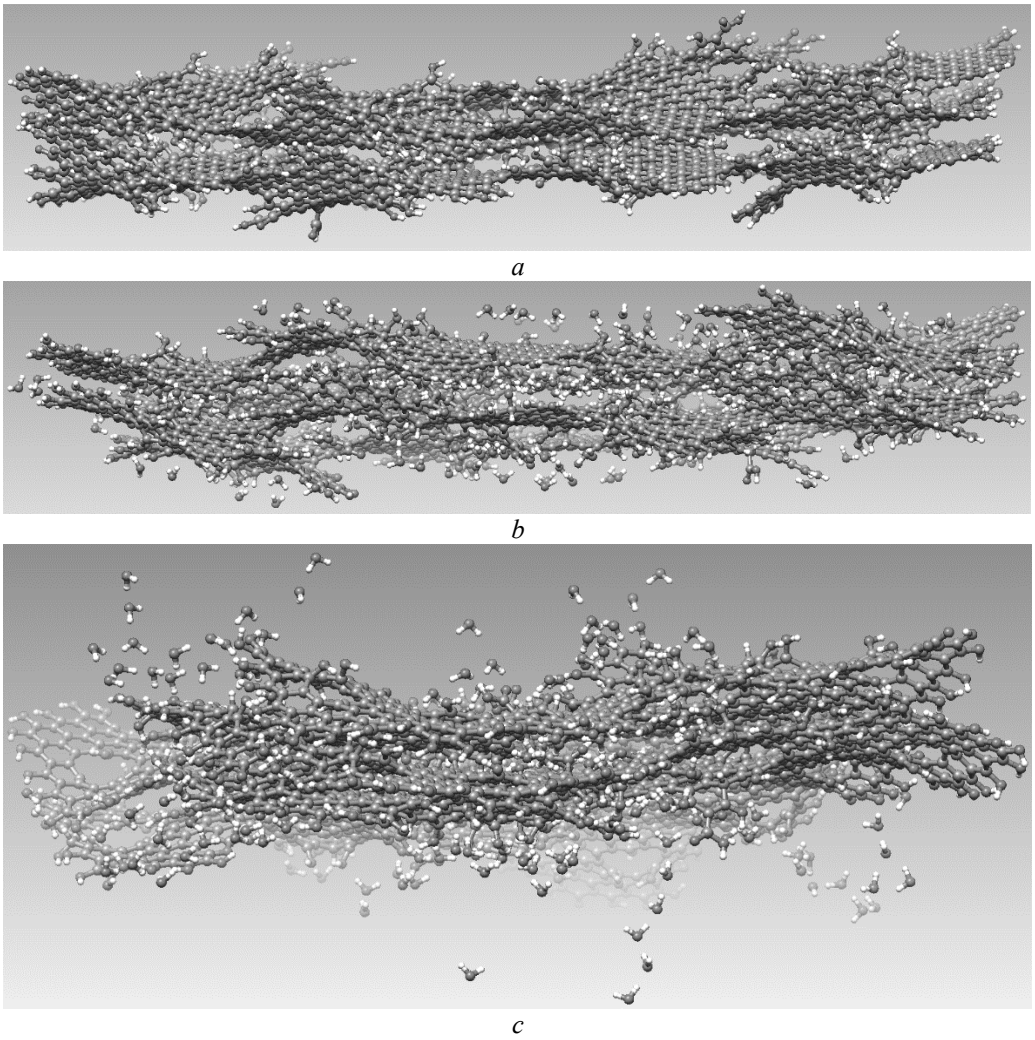

Fig. 14. Models of two–layer graphene oxide (*a*) without and (*b*, *c*) with bound water molecules calculated by (*a*, *b*) MM method with the MM+ force field and (*c*) PM7 method

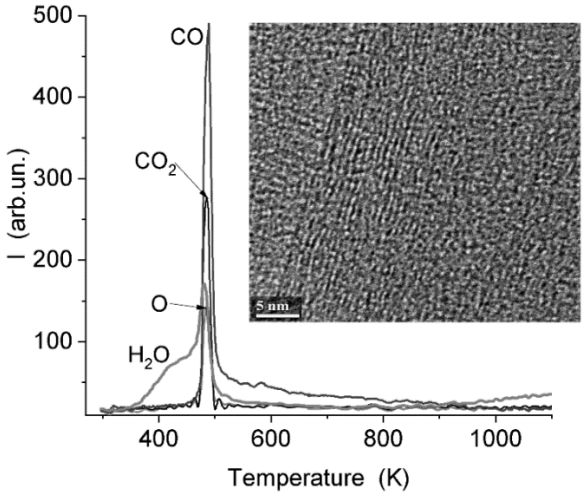

Fig. 15. OPTPD MS of degassed freeze–dry MLGO showing lines of water (*m*/*z* 18), O (*m*/*z* 16), CO (*m*/*z* 28) and CO_2 (*m*/*z* 44) (see details in [69]) (HRTEM image of MLGO in insert showing CSR of 2–10 nm in size in carbon sheet)

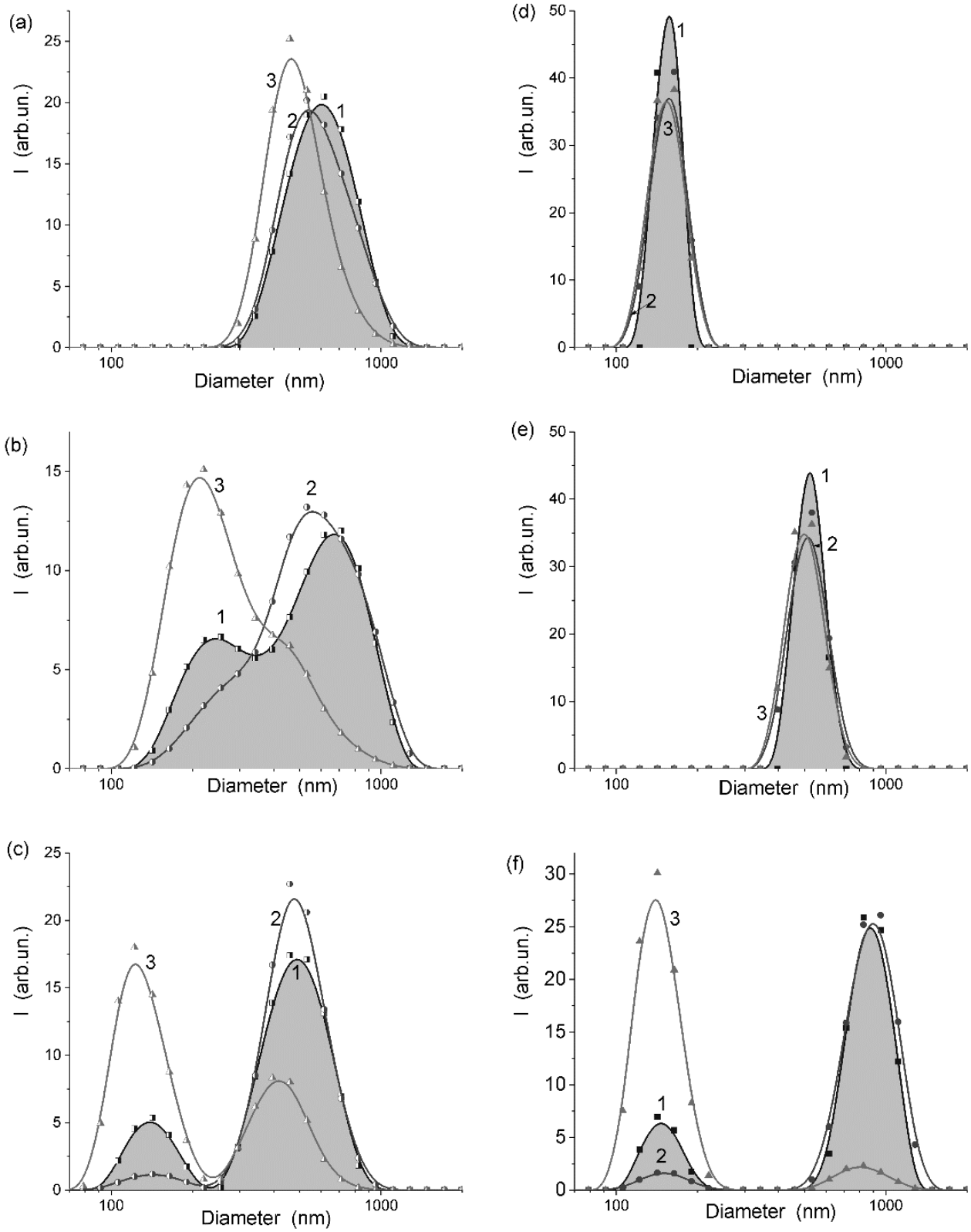

Fig. 16. Particle size distributions of MLGO at content of (*a–c*) 0.05 wt. % or (*d–f*) 0.5 wt. % and pH (*a–c*) 2.9 or (*d–f*) 2.26 sonicated for (*d*) 2, (*a*) 4, (*b*, *e*) 5, and (*c*, *f*) 10 min (curves *1*, *2* and *3* correspond to the distributions in respect to the light scattering intensity, particle volume, and particle number, respectively) (see details in [69])

The particle size distributions (PaSD) in the aqueous suspensions of freeze–dry MLGO demonstrate (Fig. 16) that an increase in the sonication time (t_{us}) of a more diluted suspension (0.05 wt. %) resulted in rather diminution of particle sizes (Fig. 16 *a*–*c*). For a more concentrated suspension (0.5 wt. %), the particle sizes increased with increasing t_{us} (Fig. 16 *d*–*f*). However, at t_{us} = 10 min the PaSD becomes bimodal (Fig. 16 *f*) due to decomposition of a fraction of secondary structures, as well as for the more diluted suspension with time t_{us} (Fig. 16 *b*, *c*). In other words, the number of smaller particles increases with increasing t_{us} value, but a fraction of larger particles includes bigger ones; *i.e.*, the processes of d_e agglomeration and agglomeration could occur in parallel. As a whole, MLGO studied demonstrated typical sizes of carbon sheets observed for commercial GO samples. This confirms that the proposed GO synthesis method using natural graphite is effective and appropriate for the MLGO preparation.

The presence of a lot of the O–containing functionalities at a surface of GO sheets provides the hydrophilic properties of the MLGO surface that cause stronger adsorption of polar water molecules than nonpolar benzene molecules (Fig. 17). However, the adsorption of water is low at $p/p_s < 0.9$ due to collapsed structure of MLGO strongly dried and degassed before the adsorption measurements. Water of a large amount can reduce sheet–sheet interactions in MLGO stacks that leads to a significant increase in the volume of pores (voids between the sheets) filled by water causing enhanced capillary condensation at $p/p_s > 0.9$. This is also due to strong swelling of MLGO since the hysteresis loop is open similar to that for preheated SLGO upon the nitrogen adsorption (Fig. 8 *a*). The swelling effects lead to an increase in the SSA value. For example, the SSA value estimated from the water adsorption branch is 35 m^2/g. However, the SSA value estimated for swollen GO from the desorption branch (p/p_s range of 0.05–0.3) is 462 m^2/g (in multipoint BET approach, and 511 m^2/g in single point BET approach). This SSA value for the swollen sample is in agreement with that for MLGO with stacks (of sheets ~ 0.5×0.5 μm^2) with 5–10 layers (Fig. 11) typical for commercial MLGO. It is in agreement with the SSA value estimated from the NMR cryoporometry data for MLGO with bound water and *n*–decane [69]. Note that the swelling effects increase for MLGO with not only adsorbed water (2 g/g) but also *n*–decane (1.5 g/g) and being in the nonpolar chloroform media but with addition of polar trifluoroacetic acid that result in the SSA value of 930 m^2/g [69].

For preheated GO, the carbon sheets with a great number of O–containing functionalities can strongly interact with neighboring sheets in dense stacks with many layers. Therefore, water molecules, which can penetrate between functionalized carbon sheets (causing the swelling effect), can be slowly desorbed in contrast to nonpolar benzene molecules, which do not penetrate between densely packed carbon sheets strongly O–functionalized (the hysteresis loop is closed for benzene, Fig. 17). This difference in the interactions of polar water and nonpolar benzene with the MLGO stacks can cause appearance of open and close hysteresis loops in the adsorption–desorption isotherms of water (more strongly interacting with MLGO, Fig. 18) and benzene (more weakly interacting with MLGO), respectively (Fig. 17).

The polar functionalities, especially acidic COOH groups, attached to carbon sheets of MLGO affect the characteristics of bound water (as well as pH of the suspensions). It is characterized by broader ^1H NMR spectra [69] than bulk free water, *e.g.*, modeled by a theoretical curve for water nanodroplet with 2000 H_2O (Fig. 18, curves *1* and *3*, respectively) due to the effects of various surface sites of GO appearing also in the theoretical curve for water bound to two-sheet model of GO (curve *2*). Deprotonation of acidic groups with the formation of cations, such as $H_5O_2^+$ or $H_9O_4^+$, results in the downfield shift of the ^1H NMR spectra of strongly associated water (SAW) at $\delta_H > 4$ ppm. Other water structures characterized by the upfield shift correspond to weakly associated water (WAW) at δ_H = 1–2 ppm due to interactions with weakly polar or nonpolar sites at the adsorbent surface [55].

Another consequence of the strong interactions between neighboring oxidized carbon sheets in the stacks of preheated, dried, and degassed GO is low adsorption of nitrogen (similar to benzene) but with open hysteresis loop (Fig. 8 *a*). However, the swelling effects of nonpolar nitrogen is much weaker than that of polar water. Therefore, the S_{BET} value of GO

estimated from the nitrogen adsorption is lower (Table 1) than that for water adsorbed onto MLGO. The SSA value for N_2 rather corresponds to the outer surface area of the MLGO microparticles. However, the benzene adsorption gives a larger value $S_{BET} \approx 15$ m^2/g than that with nitrogen, but smaller than that for water (35 m^2/g). This difference can be caused by stronger penetration of benzene molecules between carbon sheets in the MLGO stacks than nitrogen molecules can do but smaller than that for water. In the case of commercial SLGO (including particles with one–three carbon layers) degassed at 150 °C, the value of S_{BET} is very low (Table 1) comparing to the theoretical estimations (Fig. 11): the value of S_{BET} for MLGO with five carbon layer stacks in average should be about 800–900 m^2/g (it is in agreement with the NMR cryoporometry data [69]) and about 1500 m^2/g for SLGO with 1–3 layers in the stacks (Fig. 11). A large surface area can appear for MLGO studied under specific conditions in certain media [43, 69]. However, not only the dispersion medium affects the MLGO stack structure, but also MLGO affects the structure of bound liquid layers both polar (*e.g.,* water) and nonpolar (*n*–hexane or *n*–decane). This influence leads to faster evaporation of liquids in the presence of a relatively small amount of MLGO in the suspension [69]. This difference is minimal for *n*–decane (slow evaporation) and maximal for *n*–hexane (fast evaporation). The effect increases with decreasing residual amount of a liquid. This is due to an increase in the surface area at the boundary with the gas phase and easier diffusion of the molecules toward evaporation centers at a solid surface. There the energy of intermolecular interactions is smaller than that in the volume or at the surface of bulk liquid with maximal surface tension. This result can be explained by diminution of a number of neighboring molecules and increasing their disorder at the interface of a non–uniform solid surface with mosaic hydrophilic (surface hydroxyls and other O–containing functionalities) and hydrophobic (pure carbon sheet fragments without oxygen) structures. A decrease in the surface tension is confirmed by a relatively small value of γ_S of bound water [69], since it tends to decrease with decreasing amount of adsorbate [55]. Note that for all adsorbates studied on the initial stage, when the solid particles are completely immersed into the liquid, evaporation of free liquid occurs slightly faster than that for the suspension. However, as the amount of the liquid decreases and solid particles appear over the liquid surface, the evaporation is accelerated [69].

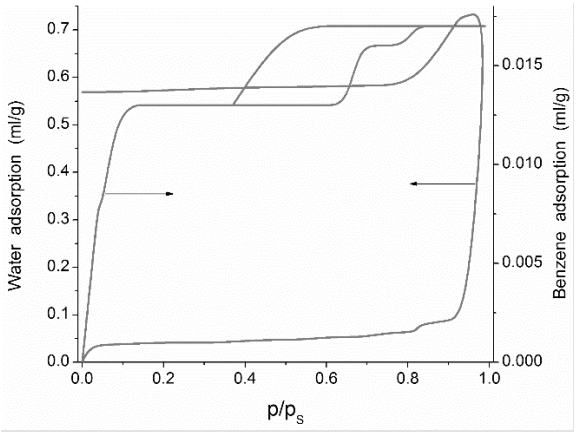

Fig. 17. Adsorption isotherms of water and benzene for freeze–dry MLGO (see details in [69])

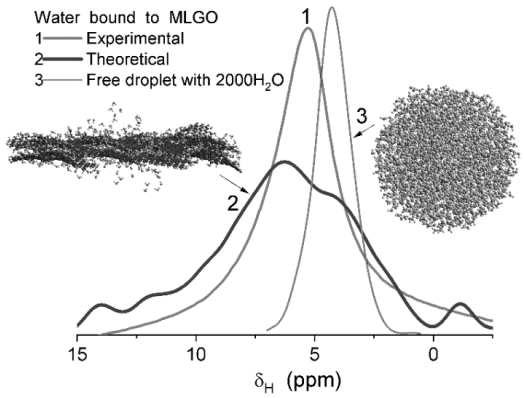

Fig. 18. ^{1}H NMR spectra of water bound to MLGO (curve *1*) experimental (12 g of water per 1 g of MLGO at 270 K) [69], theoretically calculated for water bound to MLGO (curve *2*) or free nanodroplet with 2000 H_2O (curve *3*) using the PM7 method and a correlation function linking atomic charges q_H (PM7) and the value of δ_H (calculated using GIAO/B3LYP/6–31G(d,p) for smaller systems [55]) (see details in [69])

For deeper insight into the interfacial phenomena at a surface of GO, the samples have been studied using DSC (Figs. 19–21, Table 3). The Gibbs–Thomson relation for the freezing point depression can be written upon the use of melting DSC thermograms of bound water (ice) [55,69] as follows:

$$R_p(nm) = 0.68 - k_{DSC}/(T_m - T_{m0}), \quad (1)$$

where k_{DSC} = 32.33 K nm (water) or 64 K nm (decane), T_m and T_{m0} are the melting temperatures of confined and bulk water or *n*–decane, respectively. The pore size distribution dV/dR can be calculated from the DSC melting thermograms of bound ice

$$\frac{dV}{dR}(cm^3 nm^{-1} g^{-1}) = \frac{\frac{dq}{dt}(T_m - T_{m0})^2}{k_{DSC}\rho\beta m\Delta H(T)}, \quad (2)$$

where dq/dt, ρ, β, m and $\Delta H(T)$ are the DSC heat flow, the water density, the heating rate, the sample mass and the melting enthalpy of ice, respectively. The ΔH values as a function of temperature for water can be estimated as follows

$$\Delta H(T)(\mathrm{J\ g^{-1}}) = 332 + 11.39(T_m - T_{m0}) + 0.155(T_m - T_{m0})^2. \quad (3)$$

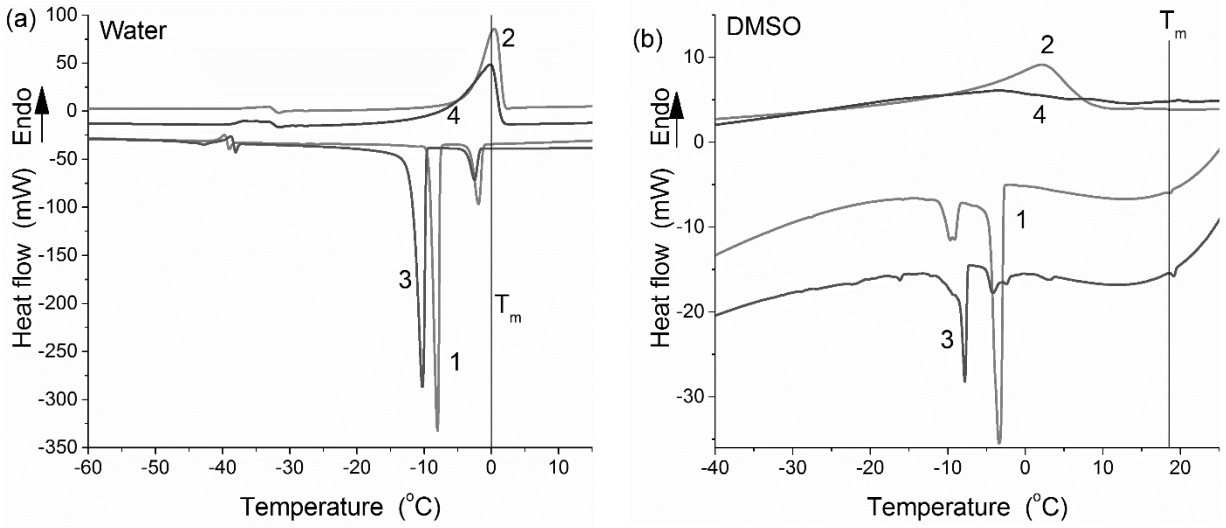

Fig. 19. DSC thermograms of polar (*a*) water (5.633 mg per 2.567 mg of MLGO or 7.047 mg per 6.782 mg of MLGO) and (*b*) dimethylsulfoxide, DMSO (5.343 mg per 1.301 mg of MLGO or 6.814 mg per 5.706 mg of MLGO) during cooling (curves *1* and *3*) and heating (curves *2* and *4*) for MLGO (*1*, *2*) freeze–dried and (*3*, *4*) dried in vacuum

An increase in relative amounts of polar (Fig. 19) or nonpolar (Fig. 20) liquids (*i.e.,* an increase in the associativity of adsorbate molecules and a decrease in the effects caused by the interfaces [55, 63]) leads to an increase in the exothermic effects during cooling and freezing of the adsorbates and endothermic effects during melting (Table 3). Note that changes in the enthalpy for bound adsorbates are smaller than those for bulk liquids for both cooling and heating (Table 3). The effect is greater for adsorbates bound to MLGO dried in vacuum than that for freeze–dry MLGO characterized by weaker collapsing effect for the stacks. The mentioned difference could be explained by strong disordering effects of oxidized GO sheet surfaces on clusters and domains of bound adsorbates both polar and nonpolar. These effects cause certain mobility of adsorbed molecules at $T < T_m$ and, therefore, certain fractions of liquids are unfrozen (at $T < T_m$). These results are in agreement with enhanced evaporation of disordered liquids in the presence of MLGO [69].

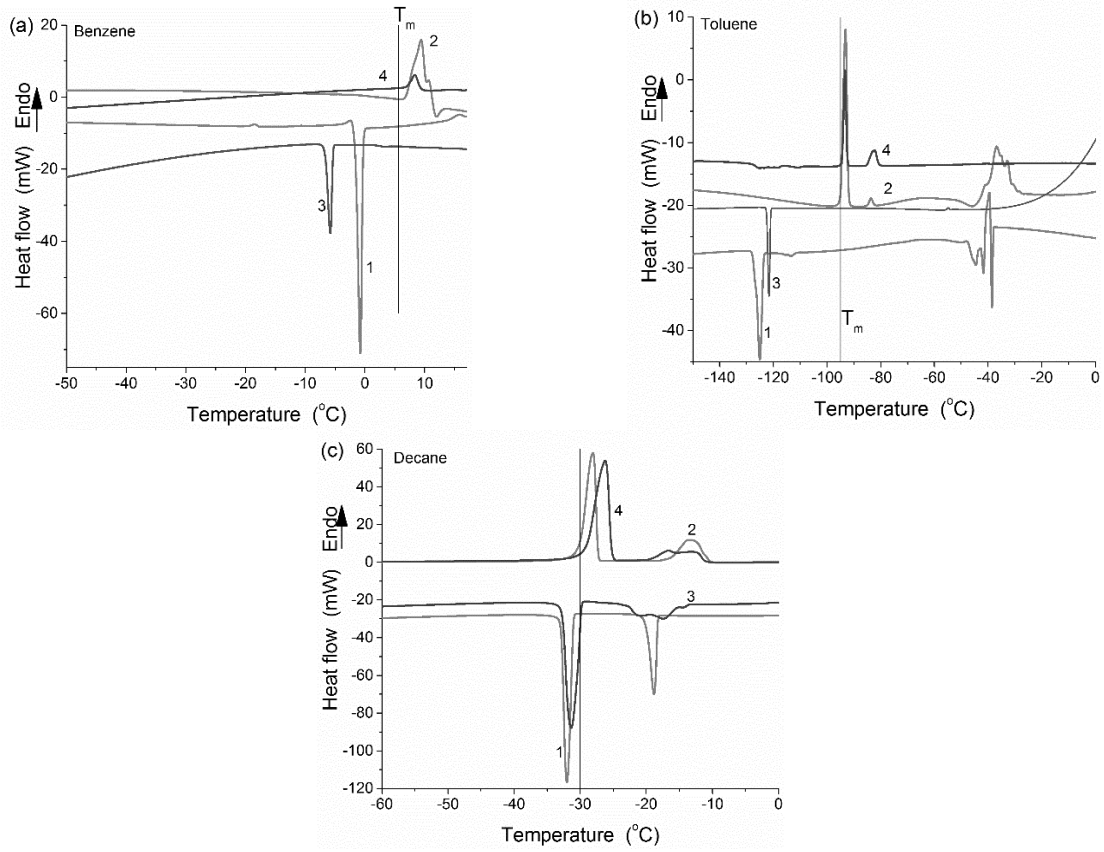

Fig. 20. DSC thermograms of nonpolar (*a*) benzene (8.978 mg per 1.99 mg of MLGO or 4.237 mg per 1.956 mg of MLGO), (b) toluene (3.878 mg per 1.524 mg of MLGO or 5.586 mg per 6.847 mg of MLGO), and (*c*) *n*–decane (3.977 mg per 2.753 mg of MLGO or 7.755 mg per 10.462 mg of MLGO) during cooling (curves *1* and *3*) and heating (curves *2* and *4*) for MLGO (*1*, *2*) freeze–dried and (*3*, *4*) dried in vacuum

The effect of delay of freezing and melting DSC peaks (*i.e.*, the hysteresis effect) with respect to the freezing–melting temperatures depends on a type of adsorbate, the amounts of both adsorbate (co–adsorbates) and adsorbent, and a cooling–heating rate. Several endotherms and exotherms can be observed (Figs. 19 and 20) due to the presence of various structures (clusters, domains) of adsorbate, which are larger or smaller, more or less ordered, and weaker or stronger interacting with the GO surface and located in pores of different sizes or on the outer surface of the carbon sheets. For water, five types of the structures such as bulk water (which does not sense the presence of an adsorbent), weakly (WBW) and strongly (SBW) bound waters (frozen close to 273 K or far from 273 K), and strongly (SAW) and weakly (WAW) associated waters (3D structures of larger sizes and 2D or branched 3D structures of smaller sizes, respectively) can be determined using DSC and NMR methods [55]. For such long and linear molecules as *n*–decane, there are additional factors related to their conformerization (due to bending of the CC–chain and rotation of the groups around the C–C bonds) and ordering–disordering of the molecules in the clusters and domains. An increase in bending of the CC–chain and disordering of the molecular clusters bound to GO lead to a decrease in intermolecular interaction energy (Table 3, ΔH). This leads to easier desorption of molecules, as well as certain changes in the shifts of the exotherms or endotherms in the DSC thermograms. These effects at the interfaces depend on the amount and strength of adsorption surface sites affecting the structure of the adsorption layers at the GO surface. Note that heating at temperatures higher that T_m (melting points) of bound liquids results in the appearance of several endotherms caused

Table 3. Shifts $\Delta T = T - T_m$ (K) in peak temperatures and corresponding enthalpy ΔH (J/g) in DSC thermograms for polar and nonpolar adsorbates bound to MLGO

Sample	Process	Adsorbates											
		DMSO		Water		Benzene		Toluene		*n*–Decane			
		ΔT	ΔH	ΔT	ΔH	ΔT	ΔH	ΔT	ΔH	ΔT	ΔH	ΔT	ΔH
MLGO (dried in vacuum)	Cooling	–14.9 –22.3 –25.8 –34.2	–0.5 –4.5 –13.6 –0.3	–2.4 –10.3	–16.6 –160.9	–11.2	–14.8	–18.4 –30.2	–0.6 –16.1	13.0	–36.4	–0.8	–97.9
	Heating	–9.5 –21.5	0.6 27.6	–0.1	156.0	2.7	5.8	12.3 1.8	0.8 21.8	13.9	28.7	4.2	104.7
MLGO (freeze–dry)	Cooling	–21.5 –27.7	–42.6 –8.2	–1.9 –7.8	–38.4 –135.7	–6.2	–18.3	–26.7	–10.6	11.7	–68.8	–2.4	–32.1
	Heating	–15.9	80.2	0.3	156.6	4.2	17.2	1.8 12.9	15.0 6.1	1.6	66.0	16.7	161.4

Note. Enthalpy of fusion at freezing point is 333.5 (water), 126.3 (benzene), 71.8 (toluene), 183.9 (DMSO), and 201.82 (*n*–decane) J/g. Values of $\Delta H < 0$ and $\Delta H > 0$ correspond to exotherms and endotherms, respectively

by changes in the organization of liquid clusters and domains and desorption of intact water (60–120 °C). Desorption of *n*–decane (boiling point $T_b \approx 174$ °C) gives a small effect (at 170–200 °C) due much smaller content of *n*–decane (0.578 mg) than water (4.509 mg) in the studied sample.

The pore size distributions, PSD (Fig. 21) calculated with the thermoporometry method [55, 69] using the DSC melting thermograms of water, *n*–decane, and water/decane at $T < T_m = 0$ °C (water) or –29.3 °C (*n*–decane) bound to GO show the effects of co–adsorption of water and *n*–decane. During co–adsorption of water and *n*–decane, water is located in larger pores of GO than in the case of the adsorption of water alone. This is typical result [55] caused by diminution of the Gibbs free energy of the system with decreasing area of contacts between such immiscible liquids as water and *n*–decane bound in different pores. This effect could lead to smaller surface area in contacts with unfrozen water bound to MLGO placed in nonpolar solventsand larger surface area in contact with *n*–decane molecules [69]. The PSD computed using *n*–decane as a probe are much narrower than that based on the water DSC curves because the Gibbs-Thomson effects of polar GO on nonpolar *n*–decane are weaker than that for polar water [55]. Therefore, melting of *n*–decane located in certain GO pores occurs in narrow temperature range. Thus, the textural changes of the GO materials depend strongly on the types of adsorbates and co–adsorbates (polarity, molecular sizes and shapes, amounts, distribution in pores between sheets in stacks, *etc*.) differently affecting the effects of swelling, adsorption, desorption, *etc*.

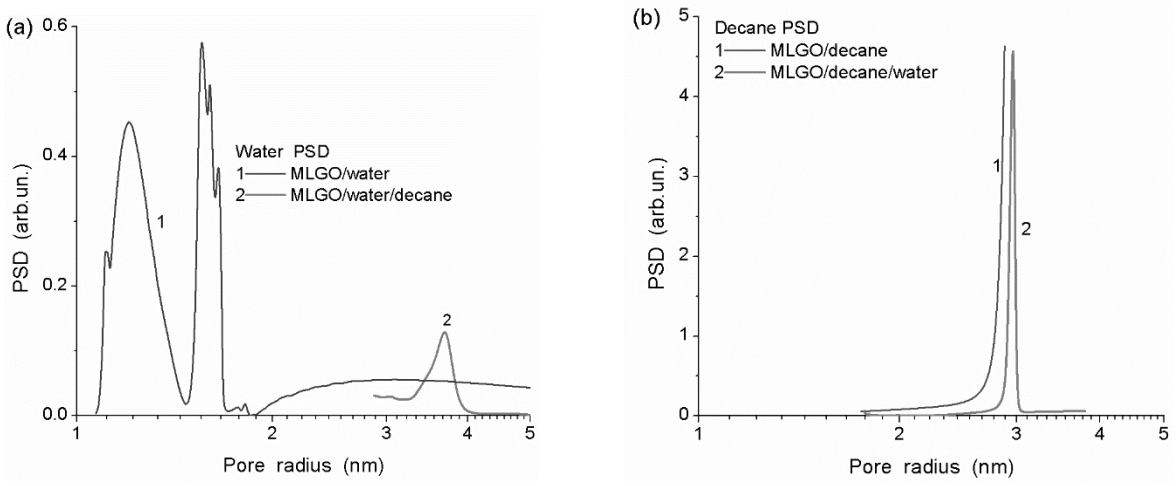

Fig. 21. Pore size distributions (PSD) calculated using DSC melting thermograms for (*a*) water and (*b*) *n*–decane bound to MLGO as water or *n*–decane alone (curve *1*) or a mixture of water and *n*–decane (curve *2*) (see details in [69])

CONCLUSION

2D carbons such as graphene oxide, graphite oxide, and exfoliated graphite demonstrate significant effects of heating, suspending–drying, cryogelation, swelling, and nitrogen, water, and organics adsorption on the morphological, structural, and textural characteristics. For example, heating at 120–150 °C results in practical collapse of pores not only between carbon sheets in the stacks but also between neighboring stacks since the SSA value decreases by a factor of 30–100 for SLGO and MLGO, since the collapse of only sheets in stacks cannot provide such great diminution of SSA. According to the XRD and HRTEM data, the GO structure is rather amorphous, since only small X-ray coherent-scattering regions are observed in sheets. The GO structure mainly amorphous but with small X-ray coherent scattering regions in carbon sheets is characterized by broad XRD (001) and (002) lines. The D line (disordered, defect structures with sp^3 hybridized C atoms, named also as diamond–like carbon) intensity for GO is similar to that of the G line (ordered structures with sp^2 hybridized C atoms, graphite–

like carbon) in the Raman spectra. The GtO structure, which is closer to that of graphite than that of GO, is characterized mainly by G line (D is very weak) in the Raman spectra, but the main XRD peak at 26.4° (characteristic for graphite) broadened similar to the XRD peak of GO at 10°.

Despite the GO stacks have a tendency to collapse upon heating, the collapsed stacks can easily swell not only in water but also in nitrogen. Thus, the use of GO in aqueous media can provide great SSA values in contact with the solvent and solute molecules and ions. This could provide high efficiency of the GO use for purification of wastewater, separation of solutes, *etc.*

MLGO produced from natural flake graphite as a precursor (flakes < 0.2 mm in size) using a modified method of ionic hydration and freeze–drying has low bulk density and typical light brown color. Interaction of MLGO with water results in strong swelling. Interaction between the carbon sheets in dry MLGO is very strong and nonpolar molecules, such as benzene, *n*–decane, *etc.*, poorly penetrate between the sheets, *i.e.*, intercalation adsorption is small, but water molecules can effectively penetrate (this is rather intercalation adsorption resulting in strong swelling) between the sheets.

Thus, the proposed synthesis method of GO using natural graphite is effective and appropriate for the MLGO preparation for various practical applications.

ACKNOWLEDGEMENT

V.M.G. is grateful to the National Research Foundation of Ukraine (Support of advanced and young scientists, grant 2020.02/0057) for financial support of this study.

2D–наноструктуровані вуглецеві матеріали: ефекти окиснення та розупорядкування пакетів

В.М. Гунько, Ю.І. Семенцов, Л.С. Андрійко, Ю.М. Ничипорук, О.І. Оранська, О.К. Матковський, Ю.В. Гребельна, Б. Хармас, Я. Скубішевська–Земба, М.Т. Картель

Інститут хімії поверхні ім. О.О. Чуйка Національної академії наук України
вул. Генерала Наумова, 17, Київ, 03164, Україна, vlad_gunko@ukr.net
Технологічний Університет Нінгбо
No 55–155 Дорога Куі Баі, Нінгбо, 315016, КНР
Хімічний факультет, Університет Марії Кюрі–Склодовської
пл. Марії Кюрі–Склодовської, 3, Люблін, 20–031, Польща

Різноманітні 2D–вуглецеві матеріали демонструють значний вплив поверхневого окиснення, нагрівання, суспендування–сушіння, кріожелювання, набухання, адсорбції полярних і неполярних сполук на морфологічні, структурні та текстурні характеристики. Нагрівання при 120–150 °C може призвести до практичного колапсу пор між вуглецевими листами в стопках та сусідніми стопками, а питома поверхня (ПП) зменшується в 30–100 разів для оксидів графену (ОГ). Структура ОГ досить аморфна, оскільки лише невеликі нанорозмірні фрагменти демонструють певне упорядкування. Крім того, інтенсивність лінії D (невпорядковані, дефектні структури з sp^3 С атомами) для ОГ подібна до інтенсивності лінії G (впорядковані структури з sp^2 С атомами) у раманівських спектрах. Структура ОГ досить аморфна, хоча і існують невеликі впорядковані кластери, тому лінії XRD (001) і (002) є доволі широкими. Структура оксиду графіту (GtO), яка ближча до структури графіту, ніж структура GO, характеризується головним чином лінією G (D дуже слабка) у спектрах комбінаційного розсіювання та основним піком XRD при 26.4° (характерним для графіту), що є широким подібно до піку XRD при 10° для ОГ. Незважаючи на те, що пакети ОГ мають тенденцію колапсувати під час нагрівання, вони можуть легко набухати не лише у воді, але й у рідкому азоті. Таким чином, використання ОГ у водних середовищах може забезпечити за рахунок набухання великі значення ПП, яка відповідає площині контактів з розчинником і молекулами чи іонами розчинених речовин. Це може забезпечити високу ефективність використання ОГ для очищення стічних вод, розділення розчинених речовин тощо. ОГ, виготовлений із природного лускатого графіту як прекурсора (пластівці < 0.2 мм) за допомогою модифікованого методу іонної гідратації та сублімаційного сушіння, має низьку насипну густину і типовий

світло–коричневий колір. Взаємодія ОГ з водою призводить до сильного набухання. Взаємодія між вуглецевими листами в сухому ОГ дуже сильна і неполярні молекули, такі як бензол, н–декан, погано проникають між листами, тобто інтеркаляційна адсорбція невелика, але молекули води можуть ефективно проникати (це скоріше інтеркаляційна адсорбція) між ними. Таким чином, запропонований метод синтезу ОГ з використанням природного графіту є ефективним і придатним для отримання ОГ для різних практичних застосувань.

***Ключові слова**: оксид графену, оксид графіту, розширений графіт, морфологічні характеристики, текстура, структура, ефекти нагрівання–охолодження–сушіння, ефекти суспендування*

REFERENCES

1. Yang R.T. *Adsorbents: Fundamentals and Applications*. (New York: Wiley, 2003).
2. Somasundaran P. (Ed.) *Encyclopedia of Surface and Colloid Science*. Third Edition. (Boca Raton: CRC Press, 2015).
3. Ahuja S. (Ed.) *Separation Science and Technology.* V. 15. (Amsterdam: Elsevier, 2022).
4. Hussain C.M. (Ed.) *Handbook of Polymer Nanocomposites for Industrial Applications*. (Amsterdam: Elsevier, 2021).
5. Ahmad A., Kumar R., Jawaid M. (Eds.) *Emerging Techniques for Treatment of Toxic Metals from Wastewater*. (Amsterdam: Elsevier, 2022).
6. Ngu L.H. *Carbon Capture Technologies*. (Amsterdam: Elsevier, 2022).
7. Moreno–Piraján J.C., Giraldo–Gutierrez L., Gómez–Granados F. *Porous Materials Theory and Its Application for Environmental Remediation*. (Cham: Springer Nature, 2021).
8. Zhang J., Terrones M., Rae C., Mukherjee R., Monthioux M., Koratkar N., Kim Y.S., Hurt R., Frackowiak E., Enoki T., Chen Y., Chen Y., Bianco A. Carbon science in 2016: Status, challenges and perspectives. *Carbon.* 2016. **98**: 708.
9. Zhuang X., Mai Y., Wu D., Zhang F., Feng X. Two–dimensional soft nanomaterials: A fascinating world of materials. *Adv. Mater.* 2015. **27**(3): 403.
10. Zhu B.Y., Murali S., Cai W., Li X., Suk J.W., Potts J.R., Ruoff R.S. Graphene and graphene oxide: synthesis, properties, and applications. *Adv. Mater*. 2010. **22**(35): 3906.
11. Soldano C., Mahmood A., Dujardin E. Production, properties and potential of graphene. *Carbon*. 2010. **48**(8): 2127.
12. Zhu Y., James D.K., Tour J.M. New routes to graphene, graphene oxide and their related applications. *Adv. Mater*. 2012. **24**(36): 4924.
13. Subrahmanyam K.S., Vivekchand S.R.C., Govindaraj A., Rao C.N.R. A study of graphenes prepared by different methods: characterization, properties and solubilisation. *J. Mater. Chem.* 2008. **18**(13): 1517.
14. Hu Y.J., Jin J.A., Zhang H., Wu P., Cai C.X. Graphene: synthesis, functionalization and applications in chemistry. *Acta Phys.–Chim. Sinica*. 2010. **26**: 2073.
15. Tang Y., Guo H., Xiao L., Yu S., Gao N., Wang Y. Synthesis of reduced graphene oxide/ magnetite composites and investigation of their adsorption performance of fluoroquinolone antibiotics. *Colloids Surf. A.* 2013. **424**: 74.
16. Hummers W.S., Offeman R.E. Preparation of graphitic oxide. *J. Am. Chem. Soc.* 1958. **80**(6): 1339.
17. Gun'ko V.M., Zaulychnyy Ya.V., Ilkiv B.I., Zarko V.I., Nychiporuk Yu.M., Ptushinskii Yu.G., Pakhlov E.M., Leboda R., Skubiszewska–Zięba J. Textural and electronic characteristics of mechanochemically activated composites with nanosilica and activated carbon. *Appl. Surf. Sci*. 2011. **258**(3): 1115.
18. Waheed A., Majeed A., Iqbal N., Ullah W., Shuaib A., Ilyas U., Bibi F., Rafique H.M. Specific capacitance and cyclic stability of graphene based metal / metal oxide nanocomposites: A review. *J. Mater. Sci. Technol.* 2015. **31**(7): 699.
19. Deng Y., Fang C., Chen G. The developments of SnO_2 / graphene nanocomposites as anode materials for high performance lithium ion batteries: A review. *J. Power Sources*. 2016. **304**: 81.
20. Warner J.H., Schäffel F., Rummeli M., Bachmatiuk A. Graphene. *Fundamentals and emergent applications*. (Waltham: Elsevier, 2013).
21. Fei Q., Wei F. (Eds.) *Advanced Hierarchical Nanostructured Materials*. First Edition. (Weinheim: Wiley–VCH Verlag GmbH & Co. KGaA, 2014).
22. Luo B., Liu S., Zhi L. Chemical approaches toward graphene–based nanomaterials and their applications in energy–related areas. *Small*. 2012. **8**(5): 630.
23. Eigler S., Hirsch A. Chemistry with graphene and graphene oxide – Challenges for synthetic chemists. *Ang. Chem. Int. Ed.* 2014. **53**(30): 7720.
24. Kim T.H., Merritt C.R., Ducati C., Bond A.D., Bampos N., Brown C.L. Bulk synthesis of graphene–like materials possessing turbostratic graphite and graphene nanodomains via combustion of magnesium in carbon dioxide. *Carbon.* 2019. **149**: 582.

25. Chua C.K., Ambrosi A., Sofer Z., Macková A., Havránek V., Tomandl I., Pumera M. Chemical preparation of graphene materials results in extensive unintentional doping with heteroatoms and metals. *Chem. Eur. J.* 2014. **20**(48): 15760.
26. Chang H., Wu H. Graphene–based nanomaterials: synthesis, properties, and optical and optoelectronic applications. *Adv. Funct. Mater.* 2013. **23**(16): 1984.
27. Bai H., Li C., Shi G. Functional composite materials based on chemically converted graphene. *Adv. Mater*. 2011. **23**(9): 1089.
28. Wang S., Minami D., Kaneko K. Comparative pore structure analysis of highly porous graphene monoliths treated at different temperatures with adsorption of N_2 at 77.4 K and of Ar at 87.3 K and 77.4 K. *Microporous and Mesoporous Materials*. 2015. **209**: 72.
29. Seehra M.S., Narang V., Geddam U.K., Stefaniak A.B. Correlation between X–ray diffraction and Raman spectra of 16 commercial graphene–based materials and their resulting classification. *Carbon*. 2017. **111**: 380.
30. Gupta S., Chatterjee S., Ray A.K., Chakraborty A.K. Graphene – metal oxide nanohybrids for toxic gas sensor: A review. *Sens. Actuators B.* 2015. **221**: 1170.
31. Yang T., Lin H., Zheng X., Loh K.P., Jia B. Tailoring pores in graphene–based materials: from generation to applications. *J. Mater. Chem. A*. 2017. **5**(32): 16537.
32. Aghigh A., Alizadeh V., Wong H.Y., Islam S., Amin N., Zaman M. Recent advances in utilization of graphene for filtration and desalination of water: A review. *Desalination*. 2015. **365**: 389.
33. Smith S.C., Rodrigues D.F. Carbon–based nanomaterials for removal of chemical and biological contaminants from water: A review of mechanisms and applications. *Carbon*. 2015. **91**(7): 122.
34. Guerrero–Fajardo C.A., Giraldo L., Moreno–Piraján J.C. Graphene oxide: study of pore size distribution and surface chemistry using immersion calorimetry. *Nanomaterials.* 2020. **10**(8): 1492.
35. Gun'ko V.M., Turov V.V., Whitby R.L.D., Prykhod'ko G.P., Turov A.V., Mikhalovsky S.V. Interactions of single and multi–layer graphene oxides with water, methane, organic solvents and HCl studied by ^{1}H NMR. *Carbon*. 2013. **57**: 191.
36. Huang Y., Zeng M., Ren J., Wang J., Fan L., Xu Q. Preparation and swelling properties of graphene oxide/poly(acrylic acid–co–acrylamide) super–absorbent hydrogel nanocomposites. *Colloids Surf. A.* 2012. **401**: 97.
37. Yao C., Zhao J., Ge H., Ren J., Yin T., Zhu Y., Ge L. Fabrication of dual sensitive titania (TiO_2)/ graphene oxide (GO) one–dimensional photonic crystals (1DPCs). *Colloids Surf. A.* 2014. **452**: 89.
38. Hunt A., Dikin D.A., Kurmaev E.Z., Boyko T.D., Bazylewski P., Chang G.S., Moewes A. Epoxide speciation and functional group distribution in graphene oxide paper–like materials. *Adv. Funct. Mater*. 2012. **22**(18): 3950.
39. Park M., Kim K.H., Kim M., Lee Y. NH_3 gas sensing properties of a gas sensor based on fluorinated graphene oxide. *Colloids Surf. A.* 2016. **490**: 104.
40. Gu D., Fein J.B. Adsorption of metals onto graphene oxide: Surface complexation modeling and linear free energy relationships. *Colloids Surf. A.* 2015. **481**: 319.
41. Low C.T.J. Electrochemical approaches to the production of graphene flakes and their potential applications. *Carbon*. 2012. **54**: 1.
42. Toda K., Furue R., Hayami S. Recent progress in applications of graphene oxide for gas sensing: A review. *Anal. Chim. Acta*. 2015. **878**: 43.
43. Kim J., Jeong E., Lee Y. Preparation and characterization of graphite foams. *J. Ind. Eng. Chem*. 2015. **32**: 21.
44. Zhou H., Ganesh P., Presser V., Wander M.C.F., Fenter P., Kent P.R.C., Jiang D., Chialvo A.A., McDonough J., Shuford K.L., Gogotsi Y. Understanding controls on interfacial wetting at epitaxial graphene: Experiment and theory. *Phys. Rev. B*. 2012. **85**(3): 035406(1–11).
45. Whitby R.L.D., Gun'ko V.M., Korobeinyk A., Busquets R., Cundy A.B., László K., Skubiszewska–Zięba J., Leboda R., Tombácz E., Toth I.Y., Kovacs K., Mikhalovsky S.V. Driving forces of conformational changes in single–layer graphene oxide. *ACS Nano*. 2012. **6**(5): 3967.
46. Yoon Y., Kyu W., Hwang T., Ho D., Seok W., Kang J. Comparative evaluation of magnetite – graphene oxide and magnetite–reduced graphene oxide composite for As(III) and As(V) removal. *J. Hazard. Mater.* 2016. **304**: 196.
47. Kurnianditia L., Ong W., Sea W., Chai S. Heteroatom doped graphene in photocatalysis: A review. *Appl. Surf. Sci.* 2015. **358**(Part A): 2.
48. Ma J., Cai P., Qi W., Kong D., Wang H. The layer–by–layer assembly of polyelectrolyte functionalized graphene sheets: A potential tool for biosensing. *Colloids Surf. A.* 2013. **426**: 6.
49. Manivel P., Kanagaraj S., Balamurugan A., Ponpandian N., Mangalaraj D. Rheological behavior and electrical properties of polypyrrole / thermally reduced graphene oxide nanocomposite. *Colloids Surf. A.* 2014. **441**: 614.
50. Duster T.A., Szymanowski J.E.S., Na C., Showalter A.R., Bunker B.A., Fein J.B. Surface complexation modeling of proton and metal sorption onto graphene oxide. *Colloids Surf. A.* 2015. **466**: 28.
51. Wu J., Chen C., Hao Y., Wang C. Enhanced electrochemical performance of nanosheet ZnO / reduced graphene oxide composites as anode for lithium–ion batteries. *Colloids Surf. A.* 2015. **468**: 17.

52. Wei Z., Barlow D.E., Sheehan P.E. The assembly of single–layer graphene oxide and graphene using molecular templates. *Nano Lett*. 2008. **8**(10): 3141.
53. Liu L., Wang L., Gao J., Zhao J., Gao X., Chen Z. Amorphous structural models for graphene oxides. *Carbon*. 2012. **50**(4): 1690.
54. Whitby R.L.D., Korobeinyk A., Gun'ko V.M., Busquets R., Cundy A.B., Laszlo K., Skubiszewska–Zięba J., Leboda R., Tombacz E., Toth I., Kovacs K., Mikhalovsky S.V. pH driven–physicochemical conformational changes of single–layer graphene oxide. *Chem. Commun*. 2011. **47**(34): 9645.
55. Gun'ko V.M., Turov V.V. *Nuclear Magnetic Resonance Studies of Interfacial Phenomena*. (Boca Raton: CRC Press, 2013).
56. Erickson K., Erni R., Lee Z., Alem N., Gannett W., Zettl A. Determination of the local chemical structure of graphene oxide and reduced graphene oxide. *Adv. Mater.* 2010. **22**(40): 4467.
57. Barroso–Bujans F., Cerveny S., Verdejo R., del Val J.J., Alberdi J.M., Alegría A., Colmenero J. Permanent adsorption of organic solvents in graphite oxide and its effect on the thermal exfoliation. *Carbon*. 2010. **48**(4): 1079.
58. Barroso–Bujans F., Cerveny S., Alegría A., Colmenero J. Sorption and desorption behavior of water and organic solvents from graphite oxide. *Carbon*. 2010. **48**(11): 3277.
59. Barroso–Bujans F., Fierro J.L.G., Alegría A., Colmenero J. Revisiting the effects of organic solvents on the thermal reduction of graphite oxide. *Thermochim. Acta*. 2011. **526**(1–2): 65.
60. Zhu K., Meng A., Wang W., Song G., Zhang M., Wei Q., Du Y., Zhang D., Li Q., Li Z. Influence of oxygen–containing groups on the photocatalytic properties of ZnO/graphene oxide composite. *Mater. Lett.* 2016. **169**: 172.
61. Ma Y., Di H., Yu Z., Liang L., Lv L., Pan Y., Zhang Y., Yin D. Fabrication of silica–decorated graphene oxide nanohybrids and the properties of composite epoxy coatings research. *Appl. Surf. Sci.* 2016. **360**(Part B): 936.
62. Liu J., Liu W., Wang Y., Xu M., Wang B. A novel reusable nanocomposite adsorbent, xanthated Fe_3O_4–chitosan grafted onto graphene oxide, for removing Cu(II) from aqueous solutions. *Appl. Surf. Sci.* 2016. **367**: 327.
63. Naghdi S., Jaleh B., Shahbazi N. Reversible wettability conversion of electrodeposited graphene oxide/titania nanocomposite coating: Investigation of surface structures. *Appl. Surf. Sci.* 2016. **368**: 409.
64. Jain R., Dhanjai, Sinha A. Graphene–zinc oxide nanorods nanocomposite based sensor for voltammetric quantification of tizanidine in solubilized system. *Appl. Surf. Sci*. 2016. **369**: 151.
65. Wang H., Gao H., Chen M., Xu X., Wang X., Pan C., Gao J. Microwave–assisted synthesis of reduced graphene oxide/titania nanocomposites as an adsorbent for methylene blue adsorption. *Appl. Surf. Sci.* 2016. **360**(Part B): 840.
66. Zhang L., He Y., Feng S., Zhang L., Zhang L., Jiao Z., Zhan Y., Wang Y. Preparation and tribological properties of novel boehmite/graphene oxide nano–hybrid. *Ceram. Int.* 2016. **42**(5): 6178.
67. Kang X.J., Zhang J.M., Sun X.W., Zhang F.R., Zhang Y.X. One–pot synthesis of vanadium dioxide nanoflowers on graphene oxide. *Ceram. Int.* 2016. **42**(6): 7883.
68. Nguyen N.S., Das G., Yoon H.H. Nickel/cobalt oxide–decorated 3D graphene nanocomposite electrode for enhanced electrochemical detection of urea. *Biosens. Bioelectron.* 2016. **77**: 372.
69. Gun'ko V.M., Turov V.V., Zarko V.I., Goncharuk O.V., Matkovsky A.K., Prykhod'ko G.P., Nychiporuk Yu.M., Pakhlov E.M., Krupska T.V., Balakin D.Yu., Charmas B., Andriyko L.S., Skubiszewska–Zięba J., Marynin A.I., Ukrainets A.I., Kartel M.T. Multi–layer graphene oxide alone and in a composite with nanosilica: preparation and interactions with polar and nonpolar adsorbates. *Appl. Surf. Sci.* 2016. **387**: 736.
70. Dovbeshko G.I., Kopan V. S., Revo S.L., Nishchenko M. M., Prikhod'ko G. P., Pyatkovskiy M. L., Sementsov Yu. I., Vestmayer M. Nanostructure of exfoliated graphite. *Phys. Met. Adv. Technol.* 2005. **27**(3): 281.
71. Kartel M., Sementsov Yu., Dovbeshko G., Karachevtseva L., Makhno S., Aleksyeyeva T., Grebel'na Yu., Styopkin V., Bo W., Stubrov Yu. Lamellar structures from graphene nanoparticles produced by anode oxidation. *Adv. Mater. Lett.* 2017. **8**(3): 212.
72. Sementsov Yu., Makhno S., Kartel M., Bo W., Dovbeshko G., Styopkin V., Nedilko S. Graphene nanoparticles and graphene nanoparticles – polyamide 12/12 composites. *Int. J. Innov. Sci. Eng. Technol*. 2017. **4**(8): 71.
73. *Fiji*. 2023. https://fiji.sc/ (version 1.54b), https://imagej.net/Local_Thickness.
74. Gun'ko V.M. Various methods to describe the morphological and textural characteristics of various materials. *Himia, Fizika ta Tehnologia Poverhni.* 2018. **9**(4): 317.
75. Gun'ko V.M. Morphological and textural features of various materials composed of porous or nonporous nanoparticles differently packed in secondary structures. *Appl. Surf. Sci.* 2021. **569**: 151117.
76. Ravikovitch P.I., Neimark A.V. Density functional theory model of adsorption on amorphous and microporous silica materials. *Langmuir.* 2006. **22**(26): 11171.
77. Gun'ko V.M., Zarko V.I., Chuikov B.A., Dudnik V.V., Ptushinskii Yu.G., Voronin E.F., Pakhlov E.M., Chuiko A.A. Temperature–programmed desorption of water from fumed silica, silica/titania, and silica/alumina. *Int. J. Mass Spectrom. Ion Process.* 1998. **172**(3): 161.
78. Pedretti A., Mazzolari A., Gervasoni S., Fumagalli L., Vistoli G. The VEGA suite of programs: an versatile platform for cheminformatics and drug design projects. *Bioinformatics.* 2021. **37**(8): 1174.

79. Pettersen E.F., Goddard T.D., Huang C.C., Meng E.C., Couch G.S., Croll T.I., Morris J.H., Ferrin T.E. UCSF ChimeraX: Structure visualization for researchers, educators, and developers. *Protein Sci.* 2021. **30**(1): 70.
80. Stewart J.J.P. *MOPAC2022* (ver. 22.06). Stewart Computational Chemistry. web: HTTP://OpenMOPAC.net.
81. Whitby R.L.D., Korobeinyk A.V., Gun'ko V. M., Wright D.B., Dichello G., Smith L.C., Fukuda T., Maekawa T., Mikhalovsky S.V., Thorpe J.R. Single–layer graphenes functionalized with polyurea: architectural control and biomolecule reactivity. *J. Phys. Chem. C.* 2013. **117**(22): 11829.
82. Gun'ko V.M. Textural characteristics of composite adsorbents analyzed with density functional theory and self–consistent regularization procedure. *Himia, Fizika ta Tehnologia Poverhni.* 2020. **11**(2): 163.
83. Howe J.Y., Rawn C.J., Jones L.E., Ow H. Improved crystallographic data for graphite. *Powder Diffr.* 2003. **18**(2): 150.
84. Acik M., Lee G., Mattevi C., Pirkle A., Wallace R.M., Chhowalla M., Cho K., Chabal Y. The role of oxygen during thermal reduction of graphene oxide studied by infrared absorption spectroscopy. *J. Phys. Chem. C*. 2011. **115**(40): 19761.

Received 29.01.2023, accepted 05.09.2023